

# **Controlling Thin Film Morphology and Polymorphism of Electro-Active Molecules Using Solution Process**

---

A Thesis

Presented to

the faculty of the School of Engineering and Applied Science

University of Virginia

---

in partial fulfillment  
of the requirements for the degree

Master of Science

by

Nan Yang

December 2017

# APPROVAL SHEET

This Thesis  
is submitted in partial fulfillment of the requirements  
for the degree of  
Master of Science

Author Signature: 杨楠

This Thesis has been read and approved by the examining committee:

Advisor: Gaurav Giri

Committee Member: Joshua J. Choi

Committee Member: Matthew J. Lazzara

Committee Member: \_\_\_\_\_

Committee Member: \_\_\_\_\_

Committee Member: \_\_\_\_\_

Accepted for the School of Engineering and Applied Science:



Craig H. Benson, School of Engineering and Applied Science

December 2017

## Abstract

Organic semiconductors (OSCs) promise the advent of flexible, transparent electronics through the use of low temperature, solution processing methods of fabricating transistors on diverse substrates, such as plastic, glass, paper, and cloth. However, one of the main limitations of organic electronics is that OSC based thin film transistors (TFTs) are limited by low charge carrier mobilities and non-uniformity between transistors. 2,7-dioctyl[1]benzohieno[3,2-b][1]benzothiophene (C8-BTBT) is a small molecule organic semiconductor that has recently reported to have charge transfer mobilities as high as  $43 \text{ cm}^2 \text{ V}^{-1} \text{ s}^{-1}$ . This OSC can also form high quality thin films by proper control of the crystalline texture and morphology, which can be used to form thin film transistors (TFTs) with uniform charge transport properties. In this study, highly crystalline, aligned C8-BTBT thin films were formed using a flow coating process termed solution shearing. Cross-polarized optical microscopy (POM) was used to study the crystal morphology and texture of the resulting thin films. In addition, grazing-incidence X-ray diffraction (GIXD) was used to study the thin film alignment, crystal packing structure and defect formation. The results show that the solution shearing process causes the thin film formation of C8-BTBT to occur in the evaporative region, where the coating process and the evaporation of the solvent occur at similar time scales. Previous work has demonstrated that solution processing conditions and different solvents may induce polymorphism in the crystal packing, another important factor determining the charge carrier mobility of TFTs. Solvent dependent polymorphism was studied in this work using GIXD. Factors that could impact polymorphism such as solvent molecular volume are discussed. Solution shearing C8-BTBT thin films at varying processing parameters not only demonstrates that fluid dynamics play an important role in the thin film morphology control, but also provides an insight for controlling polymorphism, enabling us to achieve the ultimate goal of a large-area, roll-to-roll coating process to produce organic electronics. Solution shearing method is also considered to control the deposition of metal organic frameworks (MOFs). Cu(TCNQ) was selected as the prototypical MOF, given the existence of two distinct polymorphs and good electrical and magnetic conductivities. Two Cu(TCNQ) polymorphs were synthesized and validated by X-ray diffraction and

scanning electron microscopy. Applying solution shearing to metal organic frameworks (MOFs) provides new insights in controlling properties of emerging crystalline materials and engineering functional thin film devices.

## Acknowledgements

I would like to first thank my advisor Professor Gaurav Giri for his dedicated supervision and teaching throughout the past years. I also have great appreciation for the Giri group members for their help, encouragement and advice. The research efforts in the thesis would not be possible without the support from them.

I also wish to thank Professor Joshua J. Choi and Professor Matthew J. Lazzara for serving on my committee.

Professor and Chair of Chemical Engineering, William (Bill) S. Epling provided me with advice during the conclusive phase of my Master's study. I greatly appreciate it.

I will miss the time spent in the Chemical Engineering Building, the Wilsdorf Hall, and especially the X-ray beam source 450 miles from UVA where the research group collected fancy data and learned science. I have had a good time with faculty members, staff, fellow graduate students and undergraduate students at UVA. I would like to especially thank my classmate, Mr. Preston E. Fuks, for attendance in my public defense. His appearance gave me great support.

My family members are always standing behind me. They make me aware that there are people who understand me and love me.

Part of the work in the thesis is based upon research conducted at the Cornell High Energy Synchrotron Source (CHESS) which is supported by the National Science Foundation under award DMR-1332208.

## Table of Contents

Abstract .....	i
Acknowledgements .....	iii
Table of Contents .....	iv
List of Figures .....	vi
List of Tables .....	ix
List of Abbreviations and Symbols .....	x
<b>Chapter 1. Background</b> .....	1
1.1 Organic Electronics and Solution Processing of Organic Semiconductors (OSCs) .....	1
1.2 Metal Organic Frameworks (MOFs) .....	6
<b>Chapter 2. Materials and Methods</b> .....	9
2.1 Materials .....	9
2.2 Sample Preparation: Surface Modification for Shearing Substrates .....	9
2.3 Sample Preparation: Solution Shearing of C8-BTBT .....	10
2.4 Sample Preparation: Cu(TCNQ) .....	14
2.5 A Brief Introduction to Powder X-Ray Diffraction (PXRD) .....	15
2.6 A Brief Introduction to Grazing Incidence X-Ray Diffraction (GIXD) .....	16
2.7 Data Analysis Technique for Grazing Incidence X-Ray Diffraction (GIXD) .....	17
2.8 A Brief Introduction to Cross Polarized Optical Microscopy (POM) .....	18
2.9 A Brief Introduction to Scanning Electron Microscopy (SEM) .....	19
2.10 A Brief Introduction to Brunauer–Emmett–Teller (BET) theory .....	20
2.11 A Brief Introduction to Fourier Transform Infrared Spectroscopy (FTIR) .....	20
<b>Chapter 3. Results and Discussion I: Understanding Solution-Processing Effects on the Morphology of C8-BTBT Thin Films by Using the Solution Shearing Method</b> .....	22
3.1 Characterization of C8-BTBT Thin Film Morphology by Cross-Polarized Optical Microscope .....	22
3.2 Characterization of C8-BTBT Thin Film Morphology by Grazing Incidence X-ray Diffraction .....	23
3.3 Effects of Speed and Temperature on C8-BTBT Thin Film Morphology .....	30
3.4 Effects of Concentration on C8-BTBT Thin Film Morphology .....	30
<b>Chapter 4. Results and Discussion II: Solvent Dependent Polymorphism in C8-BTBT Thin Films Studied by Using the Solution Shearing Method</b> .....	32
4.1 Solution Processing Effects on Polymorphism .....	32
4.2 Solvent Dependent Polymorphism .....	34
4.3 Challenges, limitations and pitfalls .....	34
<b>Chapter 5. Results and Discussion III: Solution Processing of Cu(TCNQ)</b> .....	43

5.1 Batch Synthesis of Two Polymorphs .....	43
5.2 BET Analysis .....	46
5.3 Thin Film Experiment .....	47
<b>Chapter 6. Conclusions</b> .....	<b>49</b>
<b>References</b> .....	<b>51</b>

## List of Figures

<b>Figure 1.1: Comparison of the band gaps for a conductor, a semiconductor and an insulator.</b> .....	2
<b>Figure 1.2: Chemical structure of C8-BTBT.</b> .....	3
<b>Figure 1.3: A summary diagram of commonly used solution processing techniques for deposition of thin films.</b> .....	4
<b>Figure 1.4: Effect of solvent molecular volume on the polymorphism of TIPS-Pentacene thin films.</b> 5	
<b>Figure 1.5: Three aspects of the ordering of thin film structure and the forces determining the ordering of molecules at different length scales.</b> .....	6
<b>Figure 1.6: Crystal structures for two prototypical MOF molecules: HKUST-1 and MOF-5.</b> .....	7
<b>Figure 1.7: Ball-and-stick view of the two Cu(TCNQ) polymorph networks.</b> .....	8
<b>Figure 2.1: Schematic diagram of the solution shearing machine for the study of solution-processing effects on C8-BTBT thin film morphology and polymorphism.</b> .....	10
<b>Figure 2.2: Schematic diagram of Bragg's law.</b> .....	15
<b>Figure 2.3: Schematic diagram of the powder X-ray diffraction (PXRD).</b> .....	16
<b>Figure 2.4: Schematic diagram of the cross polarized optical microscopy (POM).</b> .....	19
<b>Figure 2.5: Schematic diagram of the scanning action of the electron beam across sample surface.</b> 20	
<b>Figure 2.6: Schematic diagram of ATR-FTIR.</b> .....	21
<b>Figure 3.1: Cross-polarized optical microscope images of the solution-sheared C8-BTBT thin film processed at 0.5 mm/s shearing speed, 90 °C shearing temperature and a solution of 10 mg/mL C8-BTBT in toluene. (a) Optical image. (b) cross-polarized image of the same region. (c) cross-polarized image of the same region with the sample rotated by an angle. (d) cross-polarized image of a zoomed-in region. The black/white arrow represents the shearing direction. The black/white scale bar is 200 μm for (a)-(c) and 50 μm for (d).</b> .....	22
<b>Figure 3.2: Cross-polarized optical microscope images of solution-sheared C8-BTBT thin films. (a) cross-polarized image of sample sheared at 1 mm/s shearing speed, 90 oC shearing temperature and a solution of 10 mg/mL C8-BTBT in toluene. (b) cross-polarized image of the same region with the sample rotated by an angle. (c) cross-polarized image of sample sheared at 3 mm/s shearing speed, 90 oC shearing</b>	

temperature and a solution and a solution of 10 mg/mL C8-BTBT in toluene. (d) cross-polarized image of the same region with the sample rotated by an angle. The black/white arrow represents the shearing direction. The black/white scale bar is 200  $\mu\text{m}$  for all cases. .... 23

**Figure 3.3: Combination of POM and GIXD images for solution-sheared C8-BTBT thin film processed at 0.5 mm/s shearing speed, 90 °C shearing temperature and a solution of 10 mg/mL C8-BTBT in toluene.** (a) GIXD image in reciprocal space with the shearing direction parallel to the incident beam. (b) GIXD image in reciprocal space with the shearing direction perpendicular to the incident beam. (c)-(e) POM images at 20X magnification. .... 25

**Figure 3.4: Combination of POM and GIXD images for solution-sheared C8-BTBT thin film processed at 3 mm/s shearing speed, 90 °C shearing temperature and a solution of 10 mg/mL C8-BTBT in toluene.** (a) GIXD image in reciprocal space with the shearing direction parallel to the incident beam. (b) GIXD image in reciprocal space with the shearing direction perpendicular to the incident beam. (c)-(e) POM images at 20X magnification. .... 26

**Figure 3.5: Tabular summary of the effects of speed and temperature on C8-BTBT thin film morphology studied by GIXD and POM when using a solution of 10 mg/mL C8-BTBT in toluene.** Red shade represents no alignment; green shade represents alignment; blank shade represents unable to identify. For POM images, the identifiable domain width values were also marked in the corresponding cells. .... 27

**Figure 3.6: Tabular summary of the effects of speed and temperature on C8-BTBT thin film morphology studied by GIXD and POM when using a solution of 5 mg/mL C8-BTBT in toluene.** Red shade represents no alignment; green shade represents alignment; blank shade represents unable to identify. For POM images, the identifiable domain width values were also marked in the corresponding cell. .... 28

**Figure 3.7: Tabular summary of the effects of speed and temperature on C8-BTBT thin film morphology studied by GIXD and POM when using a solution of 2 mg/mL C8-BTBT in toluene.** Red shade represents no alignment; green shade represents alignment; blank shade represents unable to identify. For POM images, the identifiable domain width values were also marked in the corresponding cell. .... 29

**Figure 3.8: Schematic diagram of the two deposition regimes.** .... 30

**Figure 4.1: Line cut of the (020) Bragg peak and the integration results for studying the effect of shearing speed on polymorphism with mesitylene as the solvent.** .... 32

**Figure 5.1: PXRD pattern of Cu(TCNQ) Polymorph I.** .... 43

**Figure 5.2: PXRD pattern of Cu(TCNQ) Polymorph II.** .... 44

**Figure 5.3: SEM images of starting materials and two polymorph products in Cu(TCNQ) batch synthesis.** Top left: starting material CuI at 1000X; Top right: starting material TCNQ at 250X; Bottom

left: Cu(TCNQ) Polymorph I at 5000X; Bottom right: Cu(TCNQ) Polymorph II at 5000X; All images were taken under secondary electron mode. ....45

**Figure 5.4: ATR-FTIR spectra of two polymorph products in Cu(TCNQ) batch synthesis. ....45**

**Figure 5.5: BET surface area plot of Cu(TCNQ) Polymorph I. ....46**

**Figure 5.6: BET surface area plot of Cu(TCNQ) Polymorph II. ....47**

**Figure 5.7: SEM image Cu(TCNQ) growth on Cu foil in acetonitrile solution of TCNQ at 40 °C for 1 h. ....48**

**Figure 5.8: SEM image Cu(TCNQ) growth on Cu foil in acetonitrile solution of TCNQ at 40 °C for 4 h. ....48**

## List of Tables

<b>Table 2.1: Design of experiments and sample list for the study of solution-processing effects on C8-BTBT thin film morphology and polymorphism.</b> .....	11
<b>Table 2.2: Calculation of shearing temperature for different solvents to ensure a similar evaporation rate.</b> .....	12
<b>Table 2.3: Design of experiments and sample list for the study of solvent effects on C8-BTBT thin film polymorphism.</b> .....	13
<b>Table 2.4: Summary of common crystalline thin film morphology and representative GIXD images on a two-dimensional detector.</b> .....	17
<b>Table 4.1: Results of horizontal integration of intensity for (001) Bragg peaks</b> .....	36
<b>Table 4.2: Results of vertical integration of intensity for (111) Bragg peaks</b> .....	37
<b>Table 4.3: Results of vertical integration of intensity for (020) Bragg peaks</b> .....	38
<b>Table 4.4: Effect of temperature on polymorphism by analysis of (111) Bragg peaks</b> .....	39
<b>Table 4.5: Effect of temperature on polymorphism by analysis of (020) Bragg peaks</b> .....	40
<b>Table 4.6: Effect of concentration on polymorphism by analysis of (111) Bragg peaks</b> .....	41
<b>Table 4.7: Effect of concentration on polymorphism by analysis of (020) Bragg peaks</b> .....	42

## List of Abbreviations and Symbols

OSC	Organic semiconductor
MOF	Metal organic framework
C8-BTBT	2,7-dioctyl[1]benzothieno[3,2-b][1]benzothiophene
TIPS-pentacene	6,13-bis(triisopropylsilylethynyl)pentacene
TCNQ	7,7,8,8-tetracyanoquinodimethane
PTS	Phenyltrichlorosilane
FTS	1 <i>H</i> ,1 <i>H</i> ,2 <i>H</i> ,2 <i>H</i> -Perfluorooctyltriethoxysilane
XRD	X-ray diffraction
PXRD	Powder X-ray diffraction
GIXD	Grazing incidence X-ray diffraction
POM	Polarized optical microscopy
SEM	Scanning electron microscopy
BET	Brunauer–Emmett–Teller
FTIR	Fourier Transform Infrared Spectroscopy

# 1. Background

## 1.1 Organic Electronics and Solution Processing of Organic Semiconductors (OSCs)

Currently, in the semiconductor industry, inorganic electronic devices still occupy a large share of the market, driven by the ever-increasing demands for consumer electronics such as smartphones, laptops and TVs. Organic electronics, where organic molecules are used as the semiconductor, have not had the ability to supersede its inorganic counterparts in terms of performance. However, organic electronics have their unique advantages such as low temperature ( $< 100\text{ }^{\circ}\text{C}$ ) deposition, synthetic flexibility, compatibility with transparent and flexible substrates, and the possibility of solution processing. As such, a lot of recent research and industrial practice have been focused on utilizing organic semiconductors to engineer next-generation, high-performance devices such as organic field effect transistors (OFETs), organic light emitting diodes (OLEDs) and organic photovoltaics (OPVs) [1-8].

Semiconductors are distinguished from conductors and insulators in terms of their conductivity. For inorganic semiconductors, the energy bandgap range enables electrons to be excited into the conduction band by using an external field, and the electrons move freely to generate electrical current. For organic semiconductors (OSCs), which can be small organic molecule or polymers usually have  $\pi$  electrons for charge transport, can also become conductive when an external field is applied. The typical delocalization of  $\pi$  electrons in the presence of conjugated  $\pi$  bonds takes place along the aromatic backbone and the resulting enhancement of electronic overlap facilitates the charge transport [1, 2].

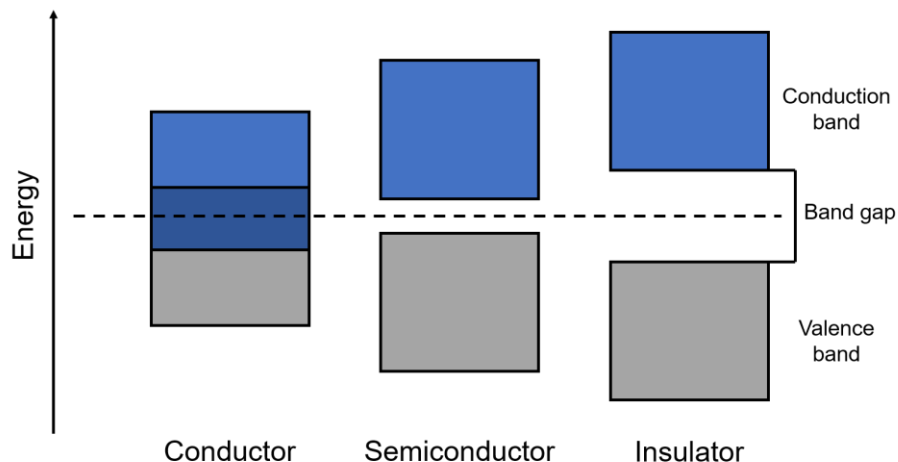


**Figure 1.1: Comparison of the band gaps for a conductor, a semiconductor and an insulator [9].**

The charge carrier mobility,  $\mu$ , is an important parameter to characterize the charge transport in semiconductors. The charge carrier mobility is defined by the speed of the charge (electron or hole) transport under an applied electric field. The charge carrier mobility can be affected by many factors at different scales. Different molecular packing of an OSC, also referred to as polymorphism, is a fundamental factor that affects charge transport rates as it changes the electronic overlap between molecules. Smaller  $\pi$ - $\pi$  stacking distance corresponds to a better electronic overlap and thus a higher charge transport rate, if all other factors are kept constant [10]. The alignment and size of the crystals as a thin film, also referred as thin film morphology, has a key effect on the charge transport of the thin film device as well. It has been experimentally proven single crystal has a superior charge carrier mobility for many OSCs, due to the lack of grain boundaries and minimized defects [11-17]. Therefore, any solution processed thin film OSCs will have the minimization of grain boundaries as a goal, in order to increase charge carrier mobility and the electrical performance of the TFT [1, 2, 18].

Metastable polymorphs of 2,7-dioctyl[1]benzohieno[3,2-b][1]benzothiophene (C8-BTBT), an OSC small molecule, have been reported using a novel off-center spin coating method, and the charge carrier mobility values were strikingly high for organic semiconductors [19-23]. Wan et al. reported two transient phases of C8-BTBT when the thin films were cast using the hollow pen writing method. In-situ grazing incidence X-

ray diffraction (GIXD) was used to capture the transient phases during the hollow pen writing process. At 85 °C, the first transient phase appeared and then disappeared while the second transient phase showed up. At 90 °C, the two transient phases were observed at the same time [24]. In-situ cross-polarized optical microscopy (POM) was used to study the thin film drying process. In this case, good thin film morphology characterized by microscopy corresponded to outstanding charge transfer mobility from measurement. At very high writing speed, they obtained large grained C8-BTBT thin films, which has practical value for the industry since large grain sizes reduce grain boundaries and thus improve electrical mobility, while creating the thin film using a fast processing method [24].

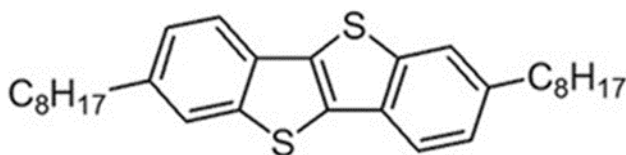


**Figure 1.2: Chemical Structure of C8-BTBT.**

Diao et al. reviewed the common thin film morphology strategies used in solution processing of organic thin film transistors. As summarized in Figure 1.3, drop-casting, spin-coating, multiple printing methods, and multiple meniscus-guided coating methods have been adopted to deposit thin films of OSCs. All meniscus-guided coating methods take advantage of balancing the rate of solvent evaporation and meniscus speed, thus directing the thin film growth during the crystallization process [25-29].

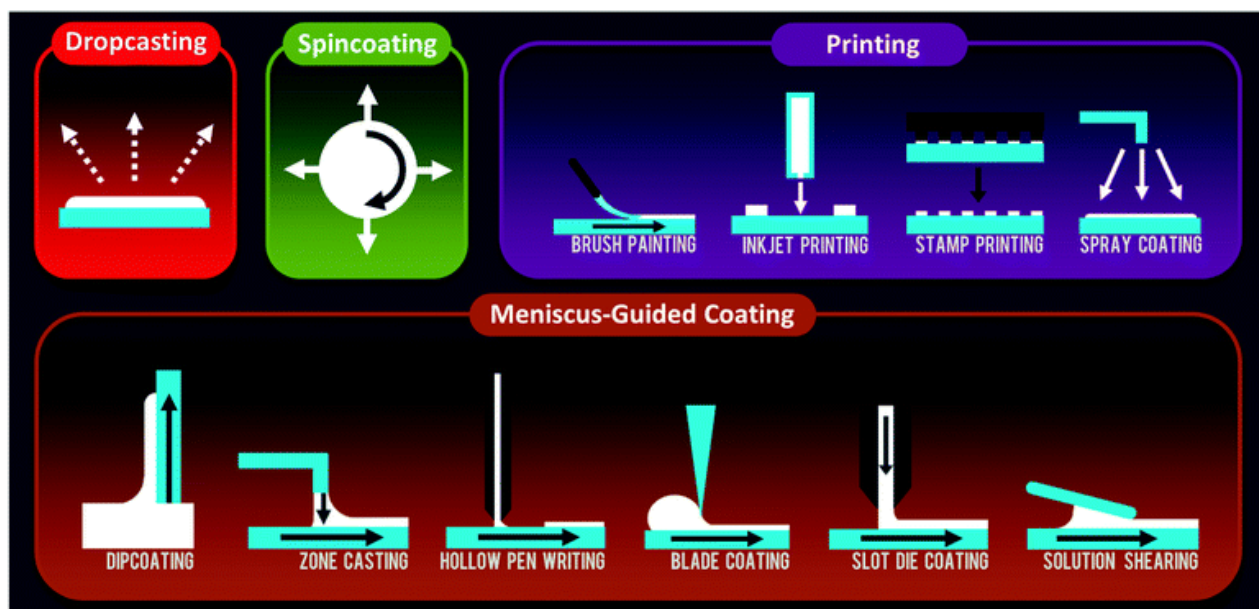


**Figure 1.3: A summary diagram of commonly used solution processing techniques for deposition of thin films [25]. - Published by The Royal Society of Chemistry.**

Giri et al. used the solution shearing method on the OSC molecule TIPS-pentacene and reported high mobility values for TFTs [30]. In their study, increasing the shearing speed was found to create metastable polymorphs with changing dimensions of the crystal lattice and shortened the  $\pi - \pi$  stacking distance, achieving higher charge transfer mobility. The improvement was not monotonic since further increase in shearing speed resulted in worsening spherulitic thin film morphology, adding more grain boundaries and defects which reduced charge transport. The mechanism for the presence of metastable polymorphs was explained as kinetic trapping during the solution shearing process [30].

In the field of pharmaceutical engineering, spatial confinement has been used to induce polymorphic behavior [31, 32]. It has been shown that spatial confinement results in the stabilization of metastable states, thus promoting the formation of various polymorphs. Giri et al. used in-situ GIXD to validate that the self-confinement hypothesis caused polymorph formation during the solution shearing of OSC molecules [33]. A metastable phase was observed during in-situ shearing and seemed coexist with the equilibrium phase after the solution shearing process was complete. It was concluded the equilibrium phase formed from the liquid-air interface and the subsequent vertical confinement from the interface to the substrate induced the

formation of the metastable phase, similar to the mechanism previously proposed for pharmaceutical molecules [33]. In light of this theory, the total thickness of the OSC film is expected to play a key role in forming polymorphs.

In Giri's work, different solvent candidates were also studied to study the effect of solvent molecular volume on the polymorphic behavior of TIPS-pentacene thin films. As shown in Figure 1.4, the (011) and (101) Bragg peaks were compared to visualize the peak shift and lattice expansion or contraction in different directions. It is proposed that the larger solvents caused molecular volume confinement, resulting in the polymorphic shifts in the packing of TIPS-pentacene [33].

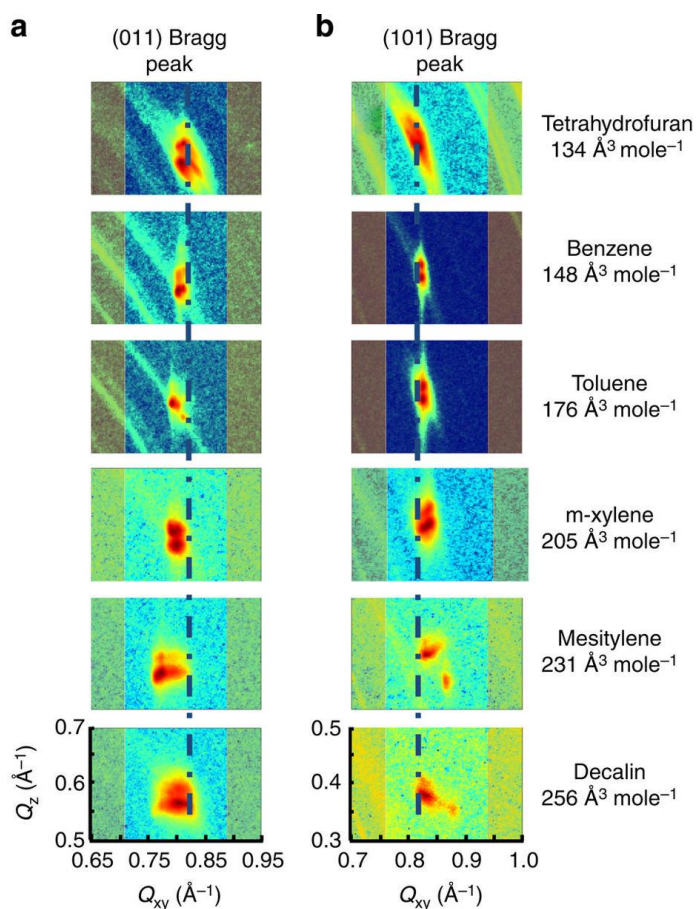


**Figure 1.4: Effect of solvent molecular volume on the polymorphism of TIPS-pentacene thin films [33]. Copyright (2014) Nature Publishing Group.**

Hiszpanski and Loo reviewed the three major aspects of thin film ordering: molecular packing in the lattice dimension (nm scale), out-of-plane molecular orientation in the film thickness (nm- $\mu$ m scale), and the in-

plane molecular orientation in the channel of the TFT ( $\mu\text{m}$  scale) [34]. Different methods were summarized for tuning the orientation at different length scales. Tuning molecular packing affects the intrinsic charge transfer mobilities of the molecules and requires understanding of the relationship between the crystal structure and the electronic properties of organic semiconductors. To control the in-plane or out-of-plane molecular orientation, tuning molecular interactions and use of external fields such as electric fields, magnetic fields, mechanical force fields and thermal gradients were mentioned as effective methods [34]. Recently Molina-Lopez et al. utilized electric field during solution shearing to tune the molecular packing and electronic properties of TIPS-pentacene and C8-BTBT thin films [35].

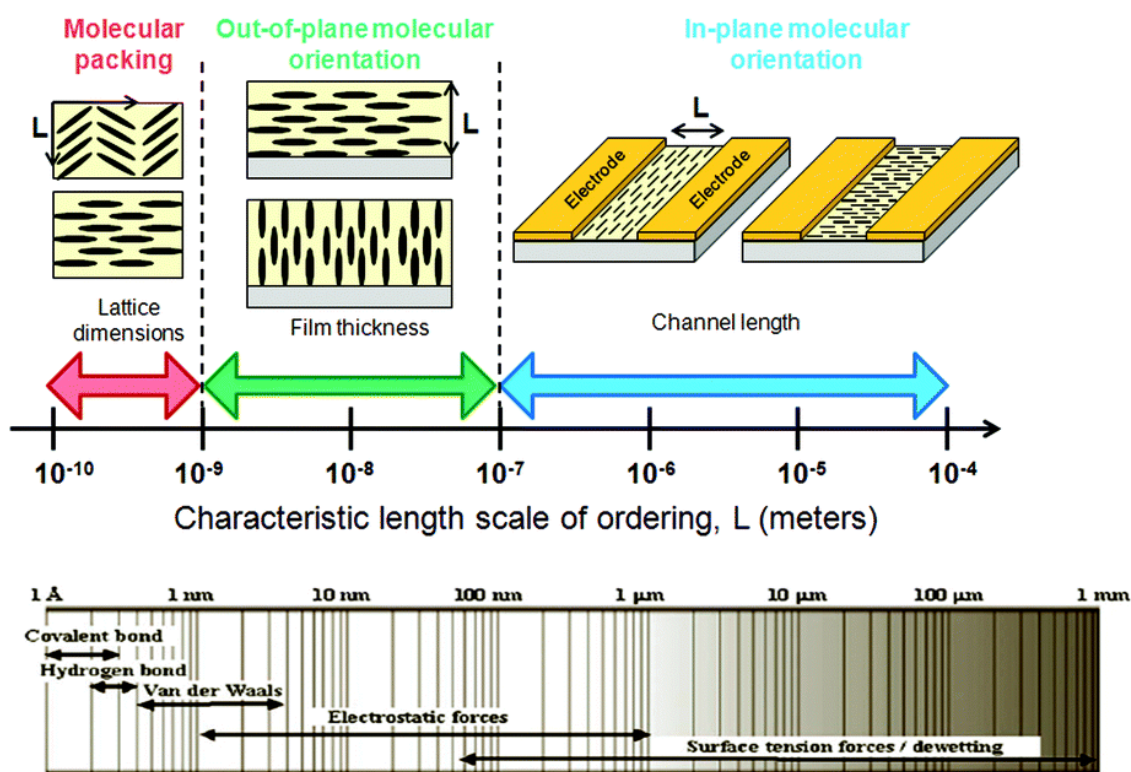
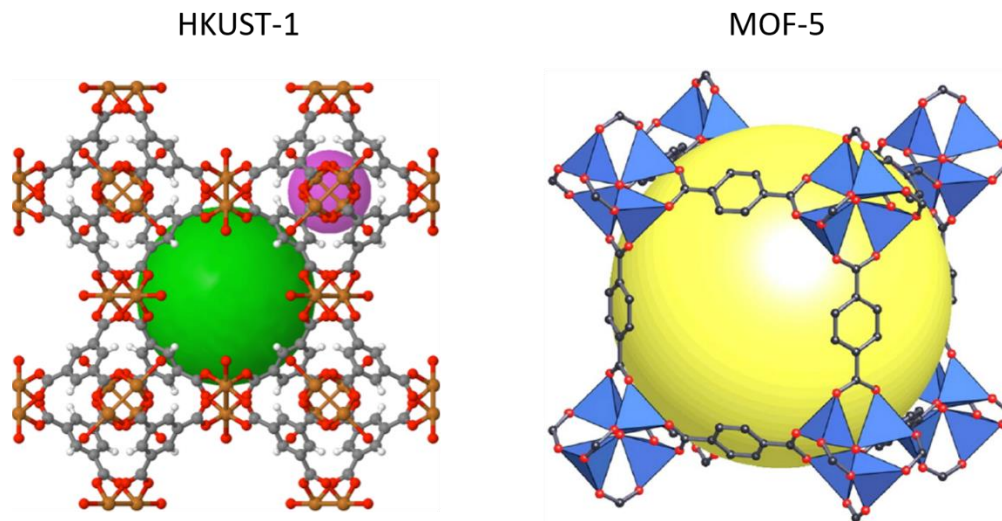


Figure 1.5: Three aspects of the ordering of thin film structure and the forces determining the ordering of molecules at different length scales. - Reproduced from Ref. [34] with formally requested permission from The Royal Society of Chemistry.

## 1.2 Metal Organic Frameworks (MOFs)

Metal organic frameworks (MOFs) are a class of coordination polymers composed of metal ions coordinated to organic ligands in an ordered, periodic manner [36-39]. Potential voids existing in the network make most MOF molecules porous, which make them extremely useful in catalysis, carbon capture and storage, and in other gas storage applications [40-47]. The application can extend to sensing, semiconductor, drug delivery when the MOF molecule has other unique properties [48-53].



**Figure 1.6: Crystal structures for two prototypical MOF molecules: HKUST-1 [54] Copyright ChemTube3D by Nick Greeves and MOF-5 [55] Copyright (2007) American Chemical Society.**

Cu(TCNQ) is a MOF where solution processing has been used to obtain two distinct phases of Cu(TCNQ), with markedly different electrical properties [56-59]. As shown in Figure 1.7, the closest distance between two independent networks of Polymorph I (right) is 3.24 Å. While in the case of the Polymorph II (left) structure, the two independent networks are interpenetrated. This difference in structure accounts for the difference in the conductivity [56, 57]. Moreover, the two polymorphs are insensitive to water and air, and do not degrade or interconvert [56-59]. In light of these futures, solution shearing method may be used to control the polymorphism of Cu(TCNQ) thin films and the ensuing electrical properties of the thin film devices.

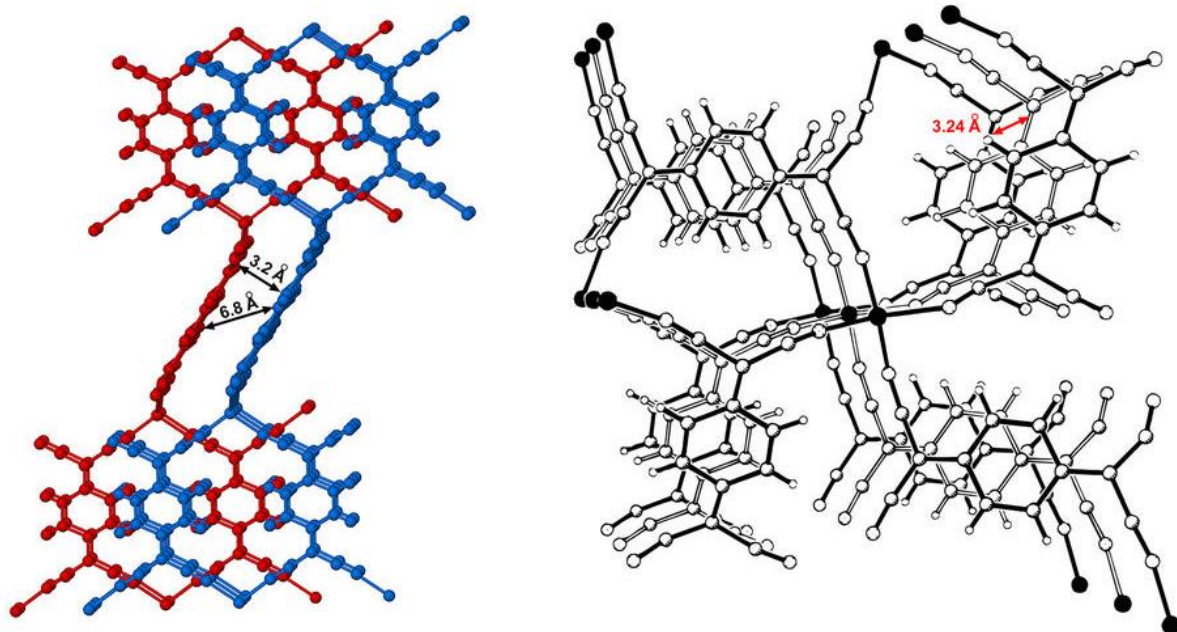


**Figure 1.7: Ball-and-stick view of the two Cu(TCNQ) polymorph networks [57]. Copyright (2014) Nature Publishing Group.**

## 2. Materials and Methods

### 2.1 Materials

C8-BTBT (received from Sigma-Aldrich) was used without further purification. Phenyltrichlorosilane (PTS) and 1*H*,1*H*,2*H*,2*H*-perfluorooctyltriethoxysilane (FTS) were purchased from Sigma-Aldrich and used as received. Highly doped *p*-type silicon wafers (4 inches in diameter, 0.005  $\Omega$  cm in resistivity, from Silicon Quest International and University Wafer, Inc.) were used as the substrates for sample preparation. Copper(I) iodide (CuI) and 7,7,8,8-tetracyanoquinodimethane (TCNQ) were purchased from Sigma-Aldrich and used as received. Copper foil was purchased from McMaster-Carr. All solvents, including toluene, acetone, isopropanol (IPA), acetonitrile, chloroform, benzene, *m*-xylene, mesitylene were purchased from Sigma-Aldrich and used as received.

### 2.2 Sample Preparation: Surface Modification for Shearing Substrates

The substrates were cut into small pieces of size  $1.5 \times 1.5 \text{ cm}^2$  and cleaned by organic solvents in the sequence of toluene, acetone and isopropanol. For the phenyltrichlorosilane (PTS) treatment, the wafers were immersed in a 3 wt% toluene solution of PTS and heated for 15 hours at 90 °C. Then the wafers were taken out of the solution and sonicated in fresh toluene for 3 minutes. The wafers were ready to use after being rinsed with aforementioned solvents in the same sequence. The water contact angle characterization showed the angle of the substrates after PTS treatment increased to 80°~85°. The purpose of the PTS treatment of the bottom substrate is to ensure enough wetting of the solution on the surface in order to improve the film quality.

For the top shearing plate, silicon wafer was cleaned by organic solvents using the aforementioned procedure and then put into a UV/ozone cleaner for 15 minutes. The 1*H*,1*H*,2*H*,2*H*-perfluorooctyltriethoxysilane (FTS) treatment was accomplished by putting the wafer into a dessicator with 15  $\mu\text{L}$  of FTS stored in an open-top vial for 3 hours. Then the wafers were taken out of the dessicator and sonicated in acetone for 5 minutes. The purpose of the FTS treatment of the top shearing plate is to form a

highly hydrophobic monolayer so that deposition of the solute molecules occurs solely on the bottom substrate. The water contact angle on the substrates after FTS treatment ranged between  $105^\circ$  to  $110^\circ$ .

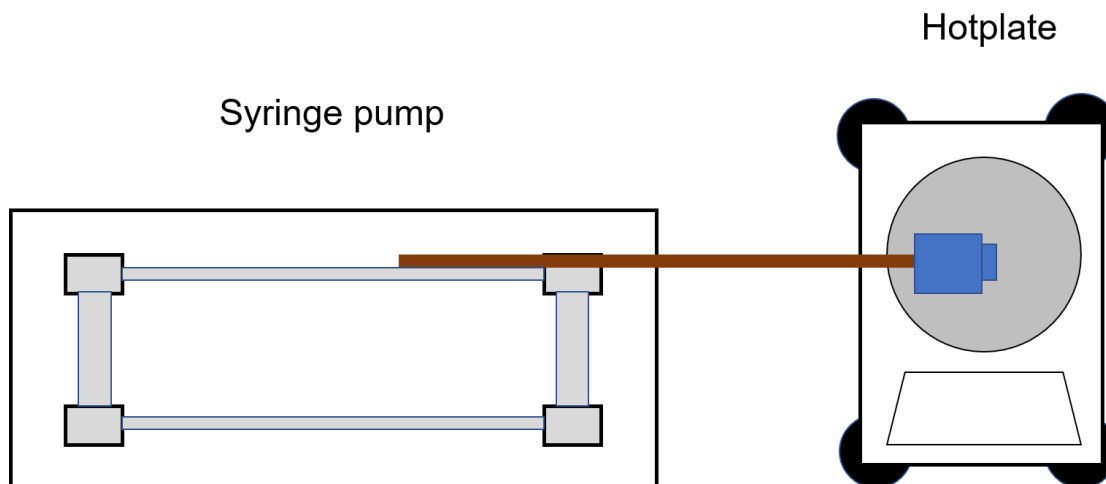


**Figure 2.1: Schematic diagram of the solution shearing machine for the study of solution-processing effects on C8-BTBT thin film morphology and polymorphism.**

### **2.3 Sample Preparation: Solution Shearing of C8-BTBT**

For the study of solution-processing effects on C8-BTBT thin film morphology and polymorphism, the C8-BTBT solution was prepared at the desired concentration (2 mg/mL, 5 mg/mL, 10 mg/mL) in toluene. The schematic diagram for the shearing machine is shown in Figure 2.1. The bottom substrate was mounted on the surface of the hot plate (from IKA) using the double-sided tape and held at the desired temperature ( $90^\circ\text{C}$  -  $30^\circ\text{C}$ ). The top plate was attached to a bar using tape with the other end attached to a syringe pump (from Harvard Apparatus). The top plate was placed on the substrate with a small area left for solution feed and a small tilt angle between  $5\sim 10^\circ$  (estimated by eye) from the horizontal. Subsequently, about  $20\ \mu\text{L}$  of solution was dropped onto the substrate and behind the end of the shearing plate using Eppendorf Pipettes. Due to capillary action, the solution went underneath the shearing plate. At the same time, the syringe pump was started to induce translation movement at the desired velocity (0.5 mm/s, 1 mm/s, 3 mm/s). When the shearing was completed the solid film was kept on the hot surface for a while to ensure the residual solvent was removed. As shown in Table 2.1, 63 samples in total were prepared to study the effects of

solution-processing parameters (speed, temperature and concentration) on the thin film morphology and polymorphism.

**Table 2.1: Design of experiments and sample list for the study of solution-processing effects on C8-BTBT thin film morphology and polymorphism.**

Shearing speed mm/s	Temperature °C	Concentration mg/mL	Shearing speed mm/s	Temperature °C	Concentration mg/mL	Shearing speed mm/s	Temperature °C	Concentration mg/mL
0.5			0.5			0.5		
1	90		1	90		1	90	
3			3			3		
0.5			0.5			0.5		
1	80		1	80		1	80	
3			3			3		
0.5			0.5			0.5		
1	70		1	70		1	70	
3			3			3		
0.5			0.5			0.5		
1	60	10	1	60	5	1	60	2
3			3			3		
0.5			0.5			0.5		
1	50		1	50		1	50	
3			3			3		
0.5			0.5			0.5		
1	40		1	40		1	40	
3			3			3		
0.5			0.5			0.5		
1	30		1	30		1	30	
3			3			3		

For the study of solvent dependent polymorphism in C8-BTBT thin films by solution shearing method, the solution shearing device was upgraded to a more automated fashion.

In this study, different temperatures are used for different solvents to ensure a similar evaporation rate. According to the experimental study by Giri et al., the ratio of the temperature divided by the boiling point at atmospheric pressure between different solvents resulted in a similar evaporation rate [33]. Table 2.2 shows the calculation of shearing temperatures for different solvents to ensure a similar evaporation rate at atmospheric pressure. Five solvent candidates were selected: chloroform, benzene, toluene, *m*-xylene and mesitylene, in the sequence of their molecular volume which is molar volume divided by Avogadro's

number, from low to high. For each solvent candidate, a high and low shearing temperature were chosen. In addition, four shearing speeds and two concentrations of C8-BTBT solution were used. Table 2.3 shows 80 samples in total were prepared to study the solvent dependent polymorphism.

**Table 2.2: Calculation of shearing temperature for different solvents to ensure a similar evaporation rate.**

Solvent	Molecular Volume $\text{\AA}^3 \text{ mole}^{-1}$	Shearing Temperature $T$ $^{\circ}\text{C}$	Boiling Point $T_b$ $^{\circ}\text{C}$	Ratio $T/T_b$ (K/K)
Chloroform	133.1	28	61.2	0.90
		45		0.95
Benzene	148.0	45	80.1	0.90
		62		0.95
Toluene	176.6	72	110.6	0.90
		91		0.95
<i>m</i> -Xylene	205.1	98	139.0	0.90
		118		0.95
Mesitylene	231.2	121	164.7	0.90
		143		0.95

**Table 2.3: Design of experiments and sample list for the study of solvent effects on C8-BTBT thin film polymorphism.**

Toluene			Chloroform			Mesitylene		
Shearing speed mm/s	Temperature °C	Concentration mg/mL	Shearing speed mm/s	Temperature °C	Concentration mg/mL	Shearing speed mm/s	Temperature °C	Concentration mg/mL
0.1	72	5	0.1	28	5	0.1	121	5
0.5			0.5			0.5		
1			1			1		
2			2			2		
0.1	91	5	0.1	45	5	0.1	143	5
0.5			0.5			0.5		
1			1			1		
2			2			2		
0.1	72	10	0.1	28	10	0.1	121	10
0.5			0.5			0.5		
1			1			1		
2			2			2		
0.1	91	10	0.1	45	10	0.1	143	10
0.5			0.5			0.5		
1			1			1		
2			2			2		

Benzene			<i>m</i> -Xylene		
Shearing speed mm/s	Temperature °C	Concentration mg/mL	Shearing speed mm/s	Temperature °C	Concentration mg/mL
0.1	45	5	0.1	98	5
0.5			0.5		
1			1		
2			2		
0.1	62	5	0.1	118	5
0.5			0.5		
1			1		
2			2		
0.1	45	10	0.1	98	10
0.5			0.5		
1			1		
2			2		
0.1	62	10	0.1	118	10
0.5			0.5		
1			1		
2			2		

## 2.4 Sample Preparation: Cu(TCNQ)

For bulk synthesis of Cu(TCNQ) Polymorph I, Heinz et al.'s method was used [56]. TCNQ (2.04 g, 10 mmol) was added into 300 mL of acetonitrile in a reaction glass bottle with a Teflon-lined cap and stirred at 60 °C, 660 rpm for 5 h. Subsequently, CuI (1.90 g, 10 mmol) was added to the hot solution and stirred for 3 min. The color of the solution turned from yellow to dark blue immediately after CuI addition. Thereafter the reaction was suspended and dark blue crystals were obtained using Buchner filtration. The filtrate was brown colored. Rinsing the product with a large amount of acetonitrile helped remove residual reactants and any by-products. Vacuum drying was used to get the final dry product.

For bulk synthesis of Cu(TCNQ) Polymorph II, a similar method was used following Heinz et al.'s procedure [56]. 3 g of Polymorph I was added to 200 mL acetonitrile. The suspension was then stirred at room temperature, 600 rpm for 4 days. The final product was obtained using Buchner filtration, rinsing with acetonitrile vacuum drying. PXRD, SEM, FTIR and other characterization techniques were also used as proof of getting Cu(TCNQ) Polymorph II.

A mechanism was proposed as acetonitrile dissolved Cu(TCNQ) I into Cu(I) and TCNQ<sup>-</sup> and then the two components recombined into a new phase which is a thermodynamically stable [56].

For the Cu(TCNQ) thin film experiments, fifteen small pieces of copper foil was cut and cleaned. Ten Cu pieces were then placed into hot acetonitrile solution of TCNQ heated at 40 °C. The other five Cu pieces were placed into hot acetonitrile solution of TCNQ heated at 80 °C. Every 1 h one piece of Cu foil was taken out of each container as the product and marked. Several products in the time-series growth or conversion experiment were characterized using PXRD and SEM to study the relevance of bulk synthesis samples to thin film samples.

Solution shearing method can also be applied to form Cu(TCNQ) thin films as an alternative method. The reactant Cu was in the state of a 20-nm thin layer on top of the silicon wafer formed by vacuum evaporation. Phase switching behavior is expected to occur when shearing acetonitrile solution of TCNQ at different

temperatures. The very thin layer of Cu is required to avoid potential damage to the GIXD detector due to the conceivable strong diffraction of Cu.

## 2.5 A Brief Introduction to Powder X-Ray Diffraction (PXRD)

X-ray diffraction is one of the most common techniques to study crystal structures. When Bragg's Law is satisfied ( $\lambda = 2d_{hkl} \sin \theta$ ), the incident X-ray beam interacts with the sample to produce constructive interference, producing diffracted beams. In a typical powder X-ray diffraction test, the detector moves around the powder while the sample holder is spinning (in the case that a sample spinner is used as the holder). The sample spinning and the random orientation of the powder ensures an isotropic diffraction pattern. The diffracted X-ray beam is recorded and counted by the detector.

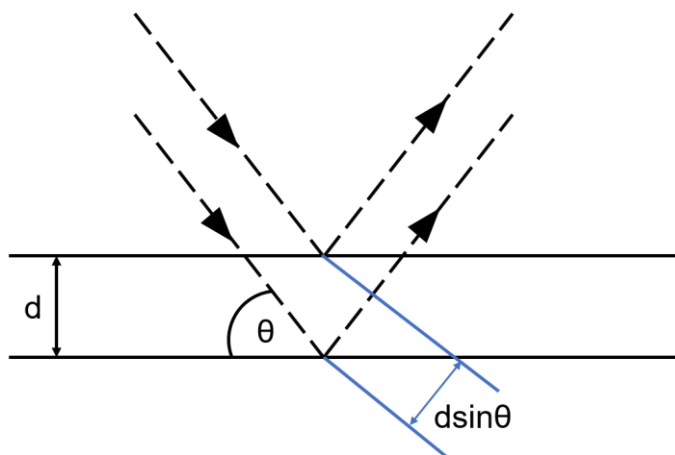


**Figure 2.2: Schematic diagram of Bragg's law [60, 61].**

Based on such principle, X-ray diffraction can be used for polymorph identification since each polymorphic phase produces a unique diffraction pattern. More advanced quantitative analyses can be extracted from the experimental XRD pattern to obtain unit cell dimensions, the microstructure of crystallites. For example, the peak position can be used to calculate interplanar distances. Moreover, the peak width can be correlated to crystallite size using the Scherrer equation.

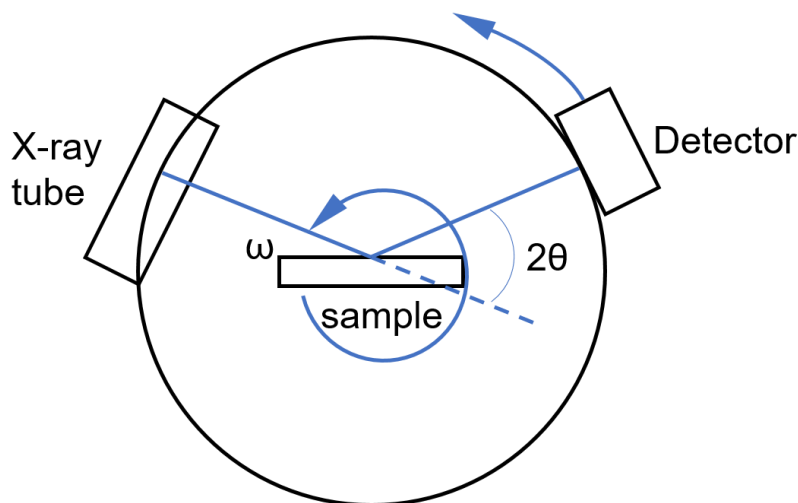


**Figure 2.3: Schematic diagram of the powder X-ray diffraction (PXRD) [62].**

The PANalytical X'Pert Pro MPD (Multi-Purpose Diffractometer) instrument located in the nanoscale materials characterization facility (NMCF) at University of Virginia (UVA) was used for the characterization of Cu(TCNQ) bulk synthesis products in the powder state and the Cu(TCNQ) thin film growth samples (sample grown on the Cu foil).

## **2.6 A Brief Introduction to Grazing Incidence X-Ray Diffraction (GIXD)**

Given the typical thickness of thin films by the solution shearing method ranges between 10 nm and 1  $\mu\text{m}$ , several issues may be encountered when using conventional XRD methods. The primary issue is that diffraction from the silicon substrate may generate a strong background signal, thus making the signal from the thin film layer hard to identify. In GIXD techniques, a small incidence angle enables the X-ray to travel across the thin to provide crystallographic information about the thin film [63].

Thin film morphology of films created by solution shearing can be readily examined using GIXD as summarized in Table 2.4. The general procedure is to obtain two GIXD patterns of the thin film by letting the beam hit the sample parallel to the shearing direction the first time and perpendicular to the shearing direction for another time. If the thin film is aligned with respect to the plane of the surface and the axis normal to the surface, different Bragg peaks may be observed. If the thin film is only aligned with respect

to the axis normal to the surface, identical Bragg peaks may show up. If the film is an isotropic powder without any alignment, the GIXD pattern may appear as concentric annular rings.

The GIXD tests for this work were conducted at the Cornell High Energy Synchrotron Source (CHESS) D1 station. The detector used was a Pilatus 200 K area detector with a pixel size of 172  $\mu\text{m}$ .

**Table 2.4: Summary of common crystalline thin film morphology and representative GIXD images on a two-dimensional detector [2, 64].**

	Schematic of alignment [64]	GIXD pattern [2]
Aligned		<p>  : Shearing direction parallel to X-ray direction;  <math>\perp</math>: Shearing direction perpendicular to X-ray direction</p>
1-D aligned in z-axis (2-D powder)		<p>  : Shearing direction parallel to X-ray direction;  <math>\perp</math>: Shearing direction perpendicular to X-ray direction</p>
Powder	Not applicable	

## 2.7 Data Analysis Technique for Grazing Incidence X-Ray Diffraction (GIXD)

For C8-BTBT polymorphism study, both the peak indexing and the peak shift observation were conducted in reciprocal space ( $q$  space). Free computational software SciLab was programmed to transform GIXD images (.tiff) from real space to reciprocal space. For each sharp peak (Bragg peak) appearing on the GIXD

image in terms of q space, values of the momentum transfer vector  $q_{xy}$  and  $q_z$  were obtained from GIXD images. Standard powder X-ray diffraction (PXRD) patterns were obtained from free crystallographic software Mercury using the crystallographic file previously published for C8-BTBT. The following equations were used to match the peak positions and index the peaks on GIXD using Miller indices (hkl).

$$q_{xyz} = \sqrt{q_{xy}^2 + q_z^2}$$

$$q_{xyz} = \frac{4\pi}{\lambda} \sin(2\theta/2)$$

$$q_{xyz} = \frac{2\pi}{d}$$

Here,  $2\theta$  was read from the PXRD peak positions.  $d$  represents the real space lattice spacing.

For the C8-BTBT solvent dependent polymorphism study, program processGIXS was used for the peak intensity integration. Horizontal and vertical line cuts was conducted to find out the peak position with maximum intensity.

## 2.8 A Brief Introduction to Cross Polarized Optical Microscopy (POM)

Cross polarized optical microscopy (POM) can be used as a direct and rapid technique to visualize morphology of thin films. The key component, the polarizer, is an optical filter that only allows light wave in the direction of the polarizer to pass through. If the light is further filtered by a second polarizer at a  $90^\circ$  angle in the propagation path then the condition is called cross polarized and the second polarizer is usually described as the analyzer. The morphology of the solution-sheared films was characterized using Zeiss AxioScope.A1 Polarized Optical Microscope. If the crystalline film is aligned, a darkness change of the single crystalline domain on the POM image is expected. If the crystalline film is not aligned with respect to the surface plane, no change in intensity is expected.

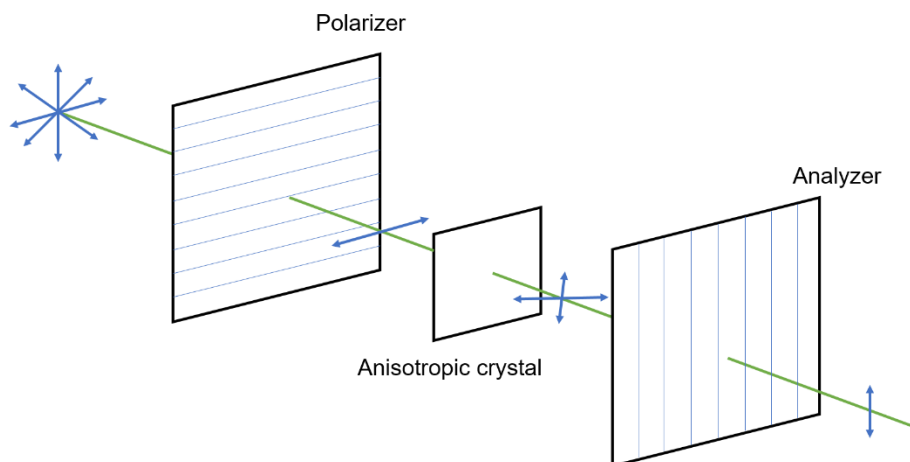


**Figure 2.4: Schematic diagram of the cross polarized optical microscopy (POM) [65].**

## 2.9 A Brief Introduction to Scanning Electron Microscopy (SEM)

SEM is a type of electron microscope based on the interaction of the electron beam with the sample surface. SEM has the advantages of higher resolving power to nanometer scale and providing topographic details. As shown in Figure 2.5, the electron beam is scanning across the sample repeatedly by hundreds to thousands of lines and secondary electrons emitted are captured by specialized detectors to produce a SEM image. FEI Quanta 650 Scanning Electron Microscope at UVA NMCF was used to characterize the morphology of the solution-sheared C8-BTBT films and Cu(TCNQ) powder and thin film samples. The second electron mode and Everhart-Thornley detector were used optimal spot size, working distance and magnification.

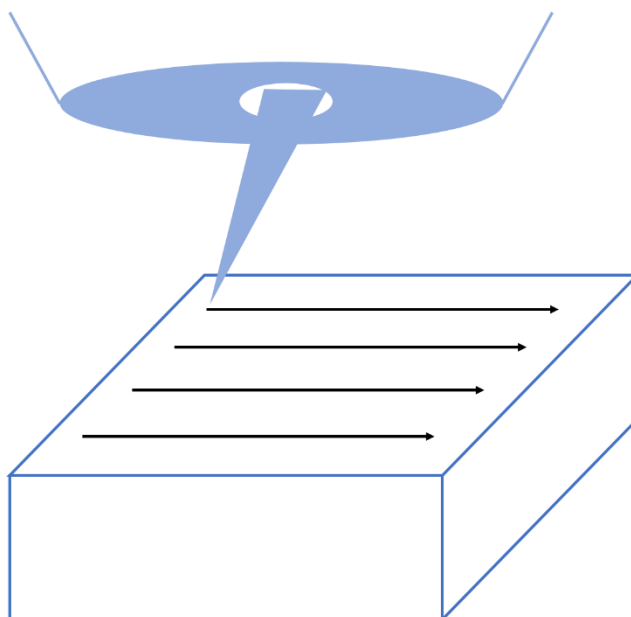


**Figure 2.5: Schematic diagram of the scanning action of the electron beam across sample surface [66].**

### **2.10 A Brief Introduction to Brunauer–Emmett–Teller (BET) theory**

The porosity and specific surface area of a porous material can be analyzed by physisorption based on the BET theory. As an extension of the Langmuir theory for monolayer adsorption and when several assumptions are met, the BET equation relates the quantity  $\frac{1}{v[(p_0/p)-1]}$  and  $p/p_0$  into a linear relationship, which can be plotted as an adsorption isotherm (also called BET plot). The specific surface area can then be calculated from the slope and intercept of the BET plot. Micromeritics ASAP 2020 Surface Area & Porosity Analyzer was used to characterize the Cu(TCNQ) powder samples. The degas condition was 120 °C for 8 h.

### **2.11 A Brief Introduction to Fourier Transform Infrared Spectroscopy (FTIR)**

FTIR is a spectroscopy technique to obtain an absorption or emission infrared spectrum from the sample. FTIR has the advantage of collecting spectra over a wide range at one time and works for solid, liquid and gas state materials. With attenuated total reflectance (ATR) technique as shown in Figure 2.6, the internal

reflectance of the IR beam occurring in the ATR crystal generates an evanescent wave that penetrates into the surface of the sample, get attenuated, return to the crystal and finally captured by the detector. ATR-FTIR makes the sample easy to test in their natural state without further preparation and generates intense IR signal. Perkin Elmer Frontier FT-MIR Spectrometer was used to characterize the Cu(TCNQ) powder samples. Diamond/ZnSe ATR and MCT detector were used.

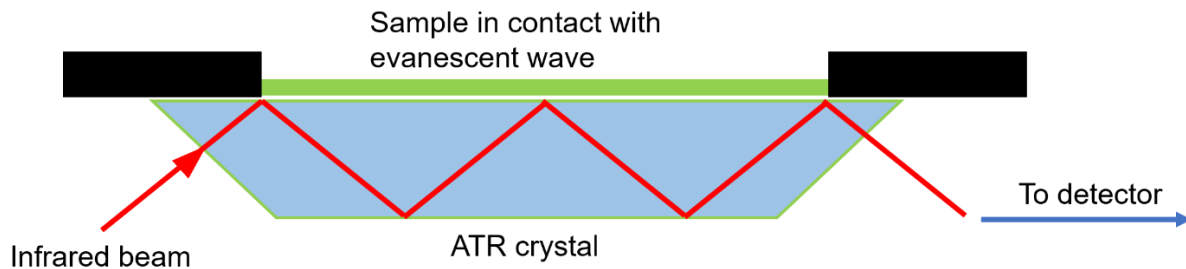


**Figure 2.6: Schematic diagram of ATR-FTIR [67].**

### 3. Results and Discussion I: Understanding Solution-Processing Effects on the Morphology of C8-BTBT Thin Films by Using the Solution Shearing Method

#### 3.1 Characterization of C8-BTBT Thin Film Morphology by Cross-Polarized Optical Microscope

Figure 3.1 shows a series of optical images taken for the solution-sheared C8-BTBT thin film processed at 0.5 mm/s shearing speed, 90 °C shearing temperature and a solution of 10 mg/mL C8-BTBT in toluene. Figure 3.1a shows a bright field image of the thin film. Here, full coverage of the film and thermal cracks were observed, but it is difficult to make out the crystal domains. Single-crystalline domains was visible under cross polarization. The difference in the darkness is caused by the relative orientation of the domain with respect to the polarizer. When the sample was rotated by a small angle, the darkness change of each domain indicates that thin film is aligned as elongated domains within the plane of the surface. Other quantitative information, such as the size of the crystal domain can also be retrieved from the polarized optical images. For this sample, the width of the domain is around several hundred microns and the length is around a few millimeters.

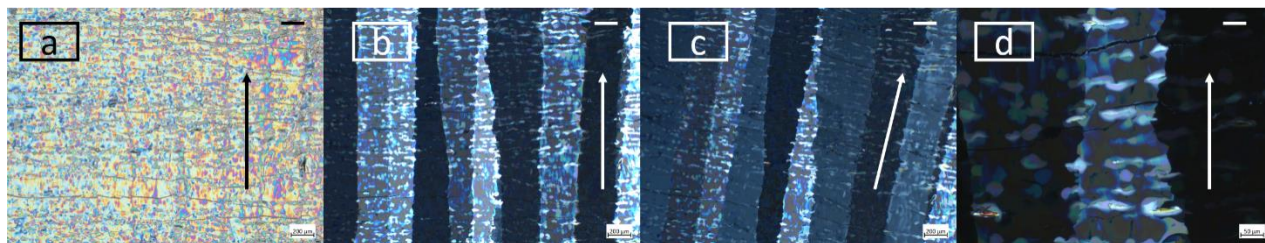


**Figure 3.1: Cross-polarized optical microscope images of the solution-sheared C8-BTBT thin film processed at 0.5 mm/s shearing speed, 90 °C shearing temperature and a solution of 10 mg/mL C8-BTBT in toluene.** (a) Optical image. (b) cross-polarized image of the same region. (c) cross-polarized image of the same region with the sample rotated by an angle. (d) cross-polarized image of a zoomed-in region. The black/white arrow represents the shearing direction. The black/white scale bar is 200  $\mu\text{m}$  for (a)-(c) and 50  $\mu\text{m}$  for (d).

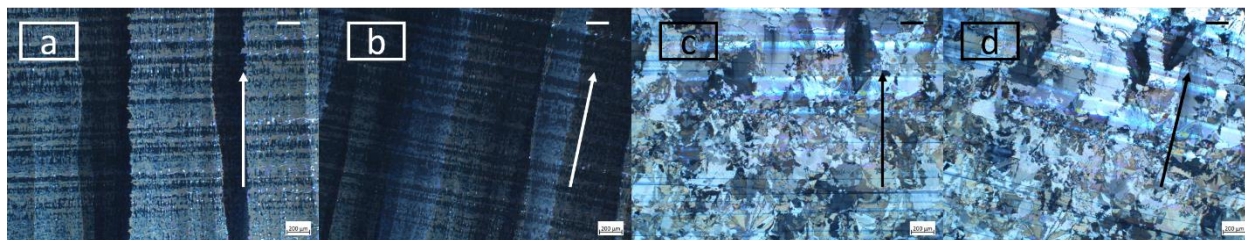


**Figure 3.2: Cross-polarized optical microscope images of solution-sheared C8-BTBT thin films.** (a) cross-polarized image of sample sheared at 1 mm/s shearing speed, 90 °C shearing temperature and a solution of 10 mg/mL C8-BTBT in toluene. (b) cross-polarized image of the same region with the sample rotated by an angle. (c) cross-polarized image of sample sheared at 3 mm/s shearing speed, 90 °C shearing temperature and a solution of 10 mg/mL C8-BTBT in toluene. (d) cross-polarized image of the same region with the sample rotated by an angle. The black/white arrow represents the shearing direction. The black/white scale bar is 200  $\mu\text{m}$  for all cases.

Figure 3.2 shows how C8-BTBT thin film morphology changes as the shearing speed increases. When the shearing speed increased from 0.5 mm/s to 1 mm/s, the size of the crystal domain decreased, which is a negative factor for charge transfer mobility. When the shearing speed further increased to 3 mm/s, the single crystalline domain disappeared and the texture of the thin film became disordered, which is very poor for electronic applications.

The thickness of the thin films can also be qualitatively evaluated. As the shearing condition approached the higher shearing speed and lower shearing temperature regime, the POM images became darker, approaching the extreme case of no coverage which corresponded to total darkness. In these cases, the capability of using POM to check thin film alignment is limited and GIXD is needed.

### 3.2 Characterization of C8-BTBT Thin Film Morphology by Grazing Incidence X-ray Diffraction

GIXD was used to characterize the alignment of the thin films. For each sample, the film was rotated parallel and perpendicular to the shearing direction. When rotating the solution-sheared C8-BTBT thin film processed at 0.5 mm/s shearing speed, 90 °C shearing temperature and a solution of 10 mg/mL C8-BTBT in toluene (by comparing Figure 3.3a and 3.3b), the array of Bragg peaks with  $q_{xy} = 13.8 \text{ nm}^{-1}$  disappears while a new array of peaks with  $q_{xy} = 8.0 \text{ nm}^{-1}$  appears, as well as the sharp peak at  $q_{xy} = 16.0 \text{ nm}^{-1}$  and  $q_z = 0$ . These Bragg peaks are caused by reflections off the (11L), (01L) and (02L) crystal planes, respectively.

This change indicates that C8-BTBT crystals are aligned with respect to the substrate, which is in agreement with the observation of POM images (Figure 3.3c-e).

By contrast, when rotating the solution-sheared C8-BTBT thin film processed at 3 mm/s shearing speed, 90 °C shearing temperature and a solution of 10 mg/mL C8-BTBT in toluene (by comparing Figure 3.4a and 3.4b), no changes in peaks are observed between the GIXD images. For example, the array of peaks with  $q_{xy} = 13.5 \text{ nm}^{-1}$  stays at the same position after sample rotation (marked by a vertical dashed line). This observation indicates that C8-BTBT crystals are isotropic with respect to the substrate, which is also in agreement with the conclusion from POM images (Figure 3.4c-e).

The three sharp peaks in the white dashed line box with  $q_{xy} = 0$  represent the (00L) Bragg peaks. For the thin film processed by the solution shearing method, the preferential alignment in the direction normal to the substrate is expected due to the fact that interface is a symmetry-breaking factor [2].

All samples sheared at 3 mm/s were found to lose in-plane alignment. This result indicates that the 3 mm/s shearing speed is too high to form aligned crystal domains, a property crucial for good electronic properties. Integrated with POM analysis, GIXD is capable of demonstrating whether the thin film is aligned or not for all samples, even if the sample is too thin for POM analysis. Almost all the results from GIXD analysis match those from POM analysis. The reason for the existence of outliers may be that non-uniform regions were scanned by the X-ray beam.

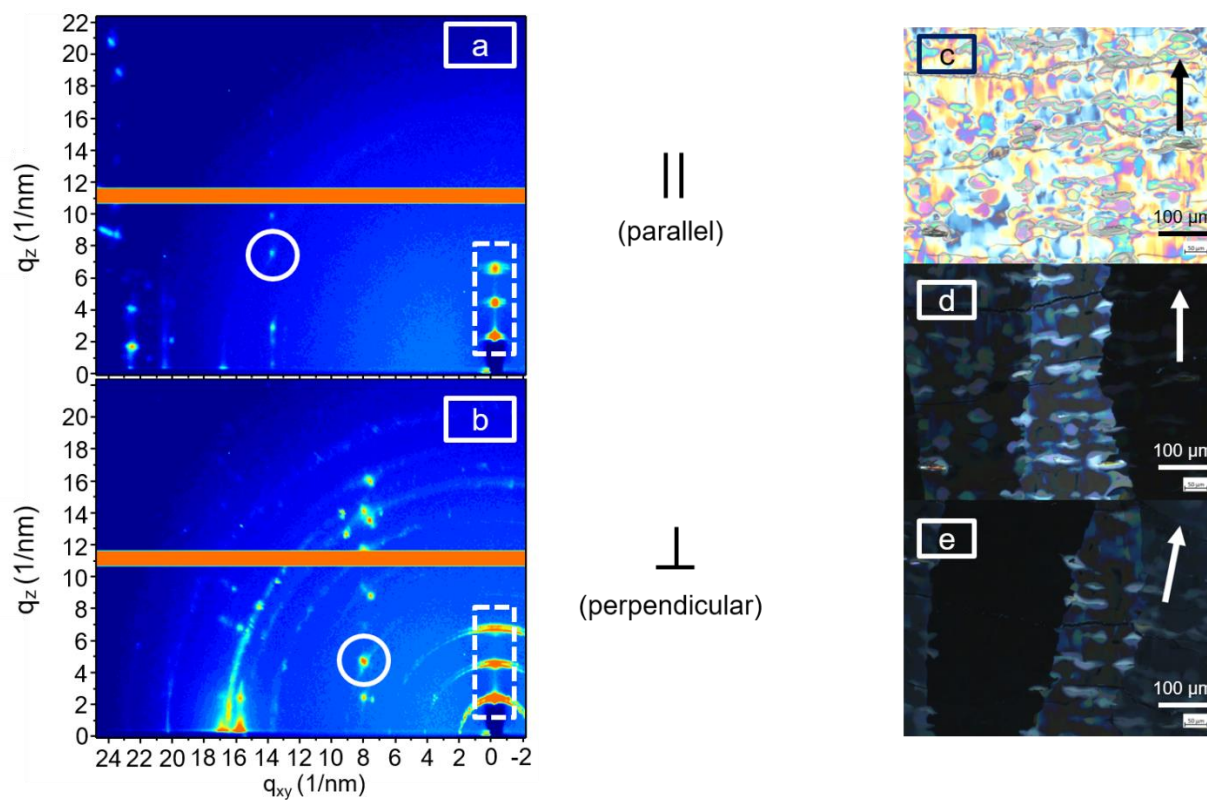


**Figure 3.3: Combination of POM and GIXD images for solution-sheared C8-BTBT thin film processed at 0.5 mm/s shearing speed, 90 °C shearing temperature and a solution of 10 mg/mL C8-BTBT in toluene.** (a) GIXD image in reciprocal space with the shearing direction parallel to the incident beam. (b) GIXD image in reciprocal space with the shearing direction perpendicular to the incident beam. (c)-(e) POM images at 20X magnification.

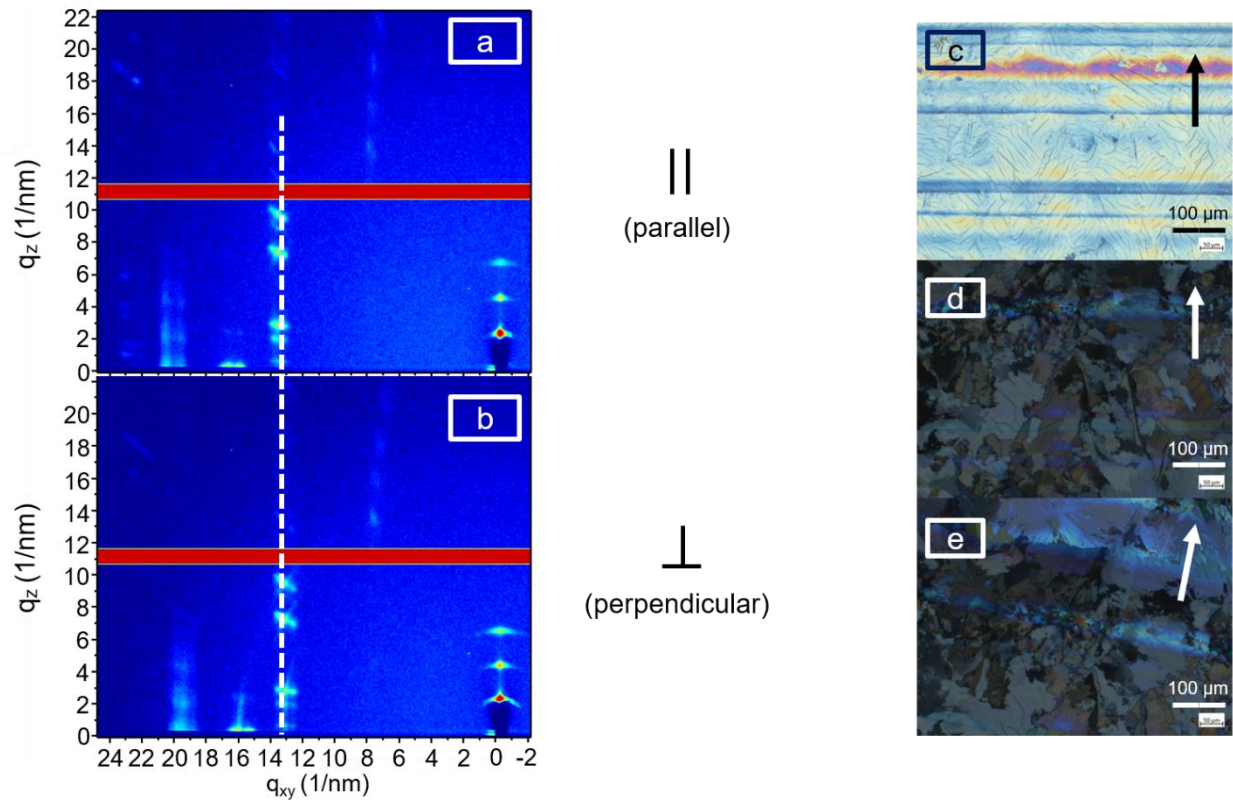


**Figure 3.4: Combination of POM and GIXD images for solution-sheared C8-BTBT thin film processed at 3 mm/s shearing speed, 90 °C shearing temperature and a solution of 10 mg/mL C8-BTBT in toluene.** (a) GIXD image in reciprocal space with the shearing direction parallel to the incident beam. (b) GIXD image in reciprocal space with the shearing direction perpendicular to the incident beam. (c)-(e) POM images at 20X magnification.

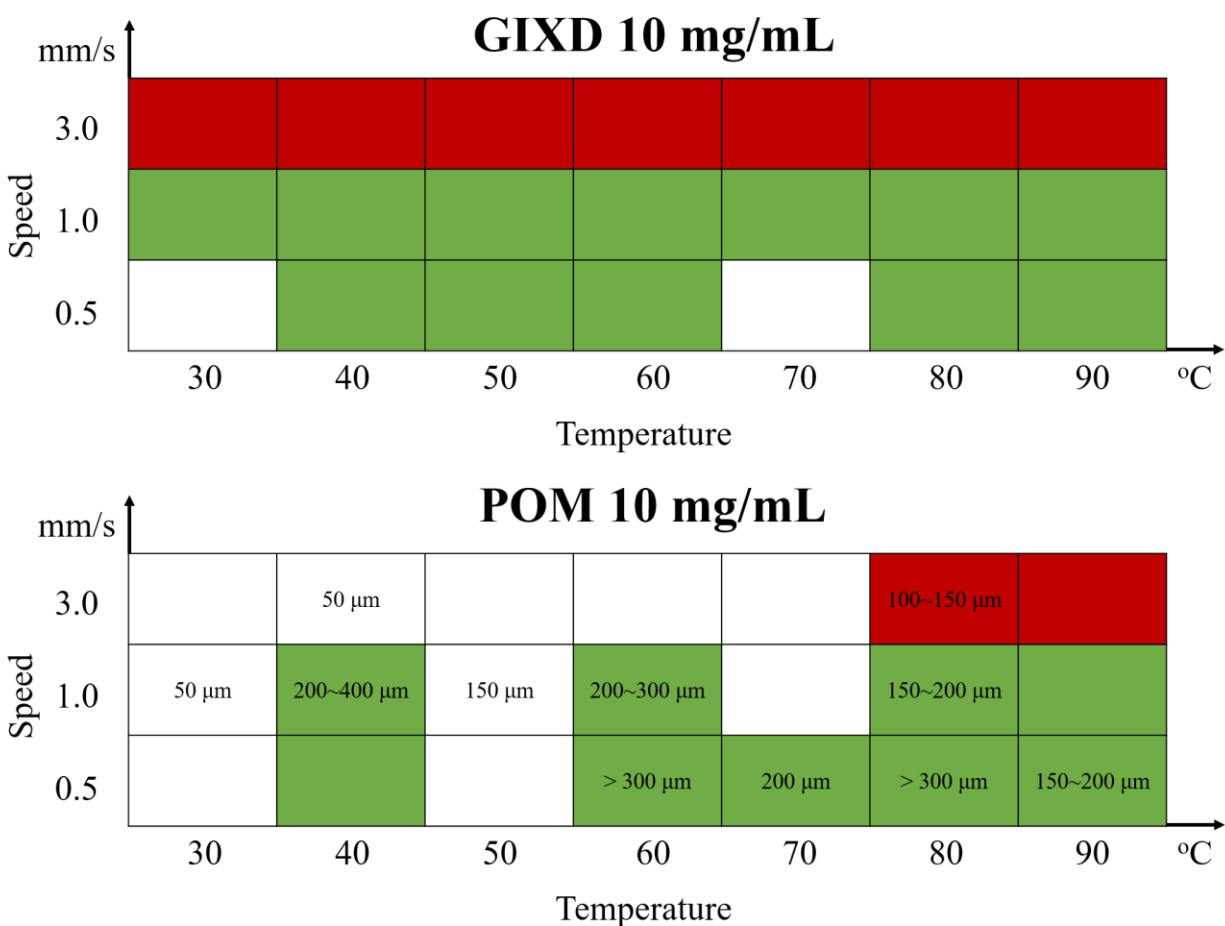


**Figure 3.5: Tabular summary of the effects of speed and temperature on C8-BTBT thin film morphology studied by GIXD and POM when using a solution of 10 mg/mL C8-BTBT in toluene.** Red shade represents no alignment; green shade represents alignment; blank shade represents unable to identify. For POM images, the identifiable domain width values were also marked in the corresponding cells.

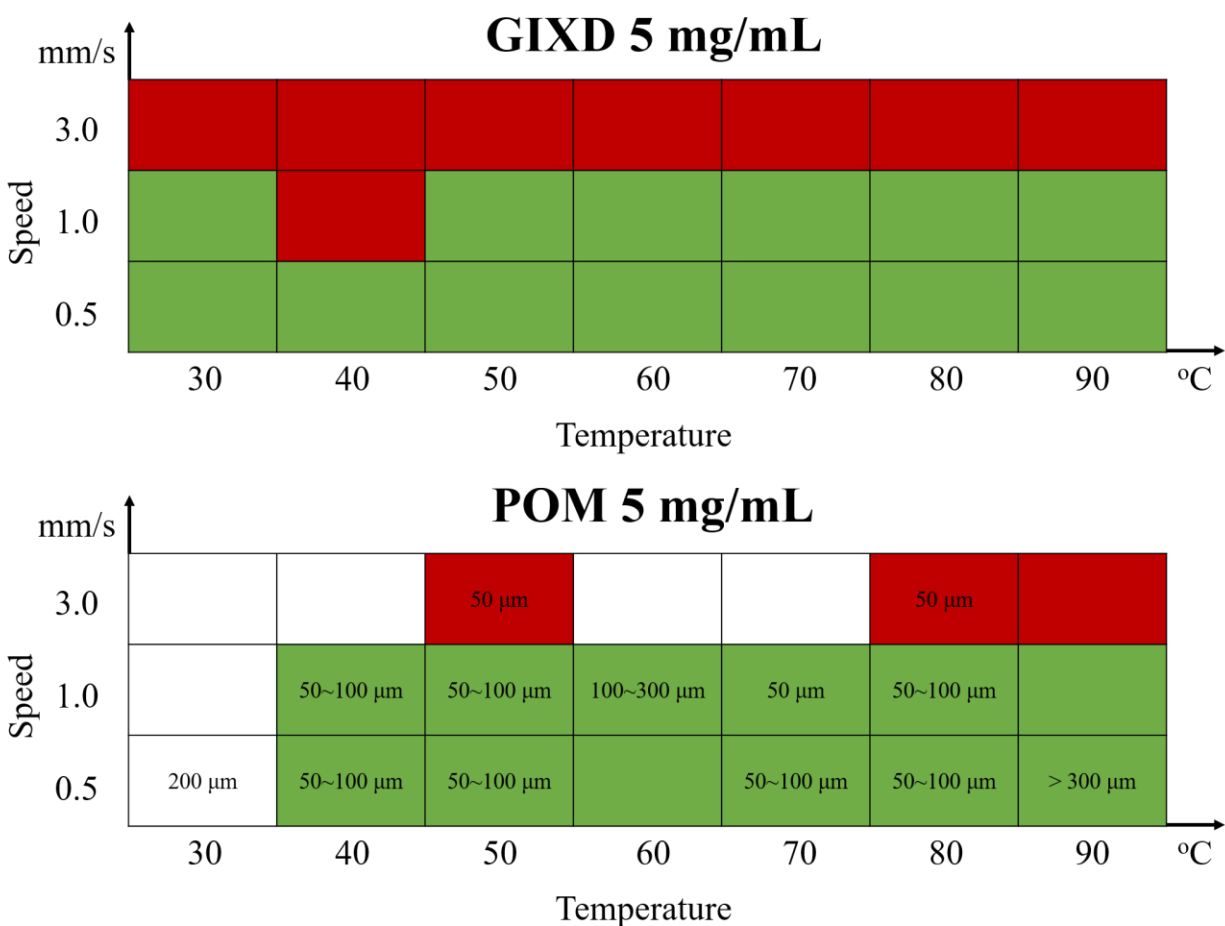


**Figure 3.6: Tabular summary of the effects of speed and temperature on C8-BTBT thin film morphology studied by GIXD and POM when using a solution of 5 mg/mL C8-BTBT in toluene. Red shade represents no alignment; green shade represents alignment; blank shade represents unable to identify. For POM images, the identifiable domain width values were also marked in the corresponding cell.**

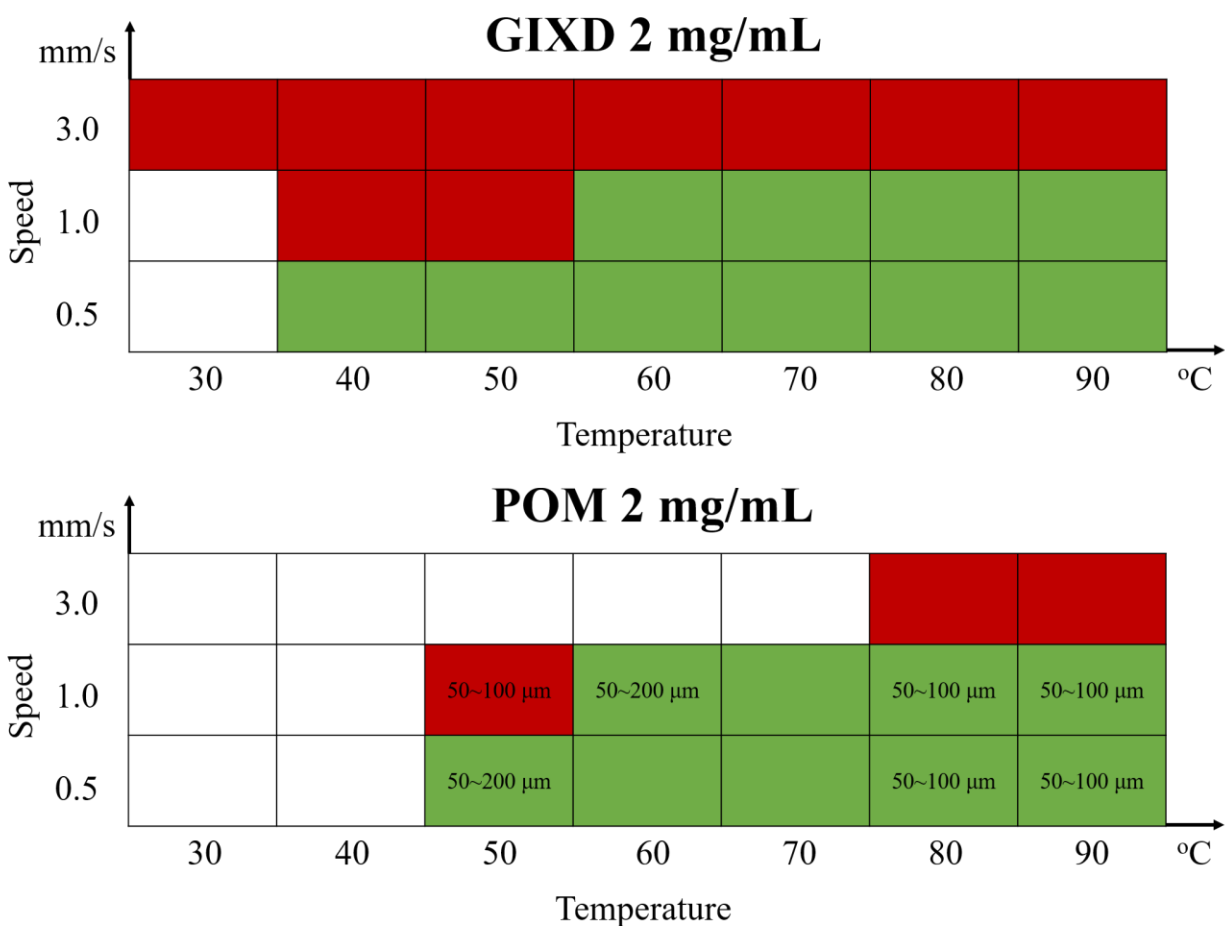


**Figure 3.7: Tabular summary of the effects of speed and temperature on C8-BTBT thin film morphology studied by GIXD and POM when using a solution of 2 mg/mL C8-BTBT in toluene. Red shade represents no alignment; green shade represents alignment; blank shade represents unable to identify. For POM images, the identifiable domain width values were also marked in the corresponding cell.**

### 3.3 Effects of Speed and Temperature on C8-BTBT Thin Film Morphology

During the solution shearing process, the film drying process and the meniscus translation process are responsible for the thin film formation. In the evaporation regime (Figure 3.8a), the two processes are coupled at similar timescales. The solution becomes concentrated as evaporation occurs, and the resulting concentration gradient forces the inflow of solvents and accompanied solutes towards the evaporation front. This transport process and resulting concentration gradient accounts for the thin film alignment along the shearing direction. On the contrary, in the Landau-Levich regime (Figure 3.8b) when the blade is moving too fast or the evaporation is too slow, the liquid film lags and dries at a slower timescale, without any benefit of fluid dynamics to cause alignment.

Based upon this theory, as the speed increased or the temperature lowered, the crystallization process approached or fell into the Landau-Levich regime, where the aligned crystal formation was negatively impacted. The theory can explain the observation that when sheared at higher shearing speed or lower temperature the C8-BTBT thin films had a tendency towards isotropy.

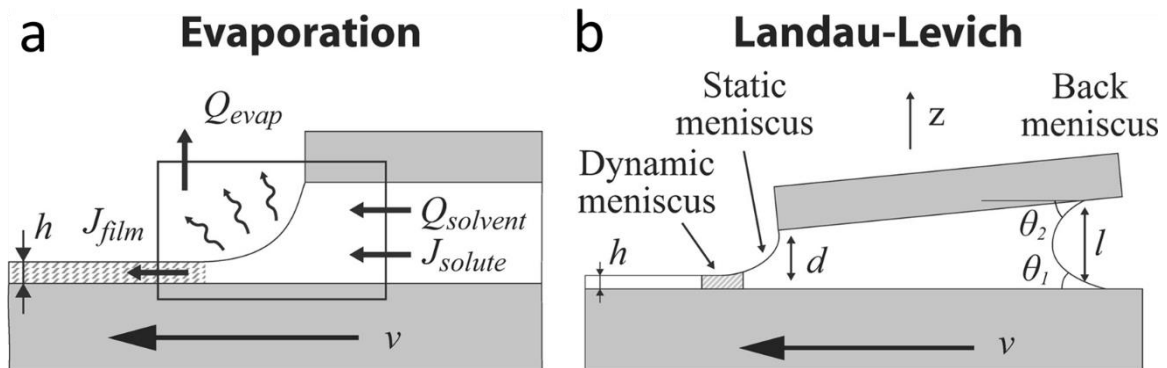


Figure 3.8: Schematic diagram of the two deposition regimes [68].

### 3.4 Effects of Concentration on C8-BTBT Thin Film Morphology

There was not an apparent trend observed regarding effects of concentration by comparing samples sheared at different concentrations. Based upon crystallization theory, the higher concentration leads to shorter time required for supersaturation, thus causing a faster rate of nucleation. The nucleation rate plays the

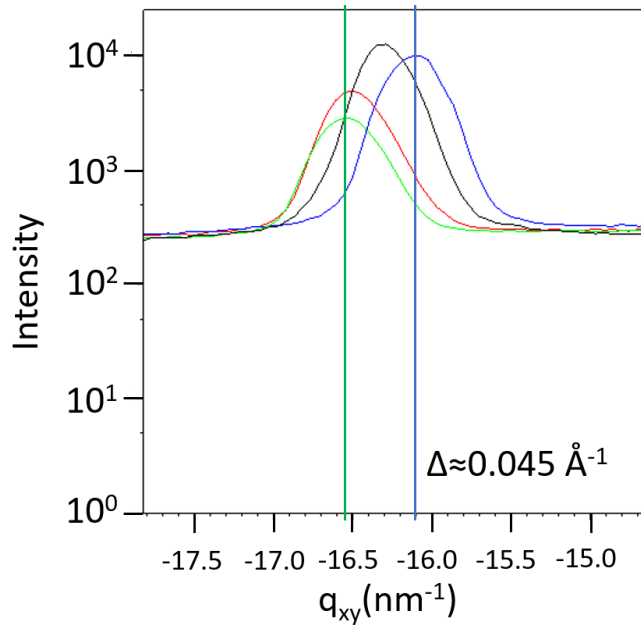
dominating role in determining the final thin film alignment. As a result, less nucleation time causes thin films sheared at higher concentration to be less aligned. However, more data at different concentration points is required to study this hypothesis.

## 4. Results and Discussion II: Solvent Dependent Polymorphism in C8-BTBT

### Thin Films Studied by Using the Solution Shearing Method

#### 4.1 Solution Processing Effects on Polymorphism

SciLab-based program ProcessGIXS was used to study the polymorphism characterized by small changes in the equilibrium crystal packing induced by solution processing conditions for each solvent candidate. As shown in Figure 4.1, a vertical integration of intensity (i.e., horizontal line cut) was applied to a region of interest surrounding a Bragg peak. The peak positions were converted to reciprocal space. Figure 4.1 is the result of the C8-BTBT (020) peak shift as a function of the shearing speed with 10 mg/mL C8-BTBT dissolved in mesitylene and sheared at 143 °C. The maximum peak shift value is about  $0.045 \text{ \AA}^{-1}$ . The peak shift pattern was not clear for these four sample.



Solvent	Mesitylene
Speed (mm/s)	0.1 <span style="color:red">—</span>
	0.5 <span style="color:blue">—</span>
	1.0 <span style="color:green">—</span>
	2.0 <span style="color:black">—</span>
Temperature (°C)	143
Concentration (mg/mL)	10

**Figure 4.1: Line cut of the (020) Bragg peak and the integration results for studying the effect of shearing speed on polymorphism with mesitylene as the solvent.**

Similar data analysis procedures were conducted for (001), (111) and (020) Bragg peaks in all samples. Since the solution sheared C8-BTBT samples were mostly aligned, only a few Bragg peaks were present

when the beam hit parallel or perpendicular to the shearing direction. Based upon the hypothesis proposed in previous study on TIPS-pentacene, the increase in shearing speed or decrease in temperature in the evaporative regime induces change in molecular packing and metastable phase formation due to self-confinement and kinetic trapping. The change in the solution concentration induces change in the thin film thickness and subsequent metastable phase formation due to vertical spatial confinement [30, 33].

In the case of the C8-BTBT crystal formed by the solution shearing method or other techniques bearing the similar mechanism, the peak shift towards the higher  $q_{xy}$  direction means a closer crystalline packing in the plane of the film and introduces a higher strain as a result [24]. A transient phase which appeared at a significantly higher  $q_{xy}$  position has been reported by Wan et al. by using in-situ GIXD technique. The transient phase was interpreted as a metastable polymorph. In the meantime, Molina-Lopez et al.'s work has pointed out two distinct polymorphs coexisting in the deposited C8-BTBT film [35]. The  $q_{xy}$  positions are  $16.1 \text{ nm}^{-1}$  and  $16.4 \text{ nm}^{-1}$  for the (020) peak, respectively. They are interpreted as both equilibrium polymorphs processed under a mild shearing condition.

The results of horizontal integration of intensity for (001) Bragg peaks are summarized in Table 4.1. From the table, it is seen that the  $q_z$  shift of the (001) peak is within a maximum range of  $0.05 \text{ nm}^{-1}$ . This change in the  $q$  value is not outstanding enough for discerning a polymorph.

The results of vertical integration of intensity for (111) Bragg peaks are summarized in Table 4.2 and those for (020) Bragg peaks in Table 4.3. By analyzing peak shifts for (111) and (020) peaks in Table 4.2 and Table 4.3, the effect of speed on polymorphism can be studied. It is seen that the peak shift induced by the speed factor in most cases are not monotonic.

The effect of temperature on polymorphism can be studied by analyzing peak shifts for (111) and (020) peaks in Table 4.2 and Table 4.3. The peak shift pattern was further summarized in Table 4.4. It is seen that the increase in temperature leads to a shift of the (111) peak to higher  $q_{xy}$  for benzene which means a closer packing and lower  $q_{xy}$  for toluene which means a farther packing. For toluene, the (020) peak shift in  $q_{xy}$

was in a reverse direction. Crystallographic analysis has revealed that there is an inverse proportional relationship between the  $q_{xy}$  of the (02L) peak and the length of  $b$ -axis of the C8-BTBT unit cell. And  $q_{xy}$  of the (11L) peak is related to the length of  $a$ -axis [35]. Thus, the difference in the shift of  $q_{xy}$  for the (111) peak and the (020) peak in the toluene case could reflect the effect of temperature differs in different dimensions of the unit cell. The polymorphic behavior could be elongation in the  $a$ -axis and contraction in  $b$ -axis when temperature increases when toluene is used as the solvent candidate. For the other solvent candidates, there is not a consistent pattern of the peak shift.

Similarly, the effect of concentration on polymorphism can be studied by analyzing peak shifts for (111) and (020) peaks in Table 4.2 and Table 4.3. The peak shift pattern was further summarized in Table 4.6 and 4.7.

#### **4.2 Solvent Dependent Polymorphism**

In addition to the study of effects of solution processing conditions, solvent dependent polymorphism was also analyzed. The pattern can be seen when looking at each row in Table 4.2 and 4.3. Each row is considered as equivalent shearing conditions for different solvent candidates.

The quantitative analysis also captured the blend of at least two C8-BTBT polymorphs under some conditions. These conditions are marked with the asterisk in Table 4.3.

#### **4.3 Challenges, limitations and pitfalls**

To study the polymorphism by solvents effects without setting the charge carrier mobility as the goal of design of experiments turned out somewhat challenging. There are enough examples by previous work showing that molecular packing is fundamental in affecting the charge carrier mobility of the thin film devices. GIXD proves to be a powerful tool to resolve the change of molecular packing in thin films, however it also has the disadvantage of the beam footprint, also known as geometric smearing, which is an apparent obstacle for polymorphism study. Geometric smearing can be avoided by shortening the length parallel to the beam hit direction. Side peaks or peak broadening in the GIXD image could be the presence

of a polymorph or just the beam footprint. More experiments need to be done to refine the sample preparation or conduct peak deconvolution for such cases.

In addition, the assumption that the evaporation rate is kept the same solely by setting the deviation of shearing temperature by boiling point in Kelvin unit equal does not strictly stand by any theoretical basis. Rather the assumption is based on experimental observation without absolute accuracy to guarantee the same evaporation rate. It is conceivable that as long as the film thickness varies in samples using different solvents, the vertical spatial confinement may exert some influence and cannot be neglected in tuning the molecular packing.

Even for the same sample, the peak shift can also be observed, and in some cases the magnitude of such shift can compare that of the maximum shift induced by solution processing conditions.

The above issues all require researchers to draw conclusions with caution with respect to both qualitative and quantitative analysis on the solvent dependent polymorphism.

**Table 4.1: Results of horizontal integration of intensity for (001) Bragg peaks**

Concentration (mg/mL)	Shearing Temperature (°C)	Shearing Speed (mm/s)	Peak position Chloroform (nm <sup>-1</sup> )	Peak position Benzene (nm <sup>-1</sup> )	Peak position Toluene (nm <sup>-1</sup> )	Peak position m-Xylene (nm <sup>-1</sup> )	Peak position Mesitylene (nm <sup>-1</sup> )
5	Low Ratio $T/T_b$ (K/K) = 0.90	0.1	2.01	2.06	2.01	2.06	2.01
		0.5	2.06	2.01	2.06	2.06	2.06
		1.0	2.06	2.04	2.06	2.06	2.06
		2.0	2.01	1.95	2.06	2.01	2.01
	High Ratio $T/T_b$ (K/K) = 0.95	0.1	2.01	2.01	1.96	2.01	2.01
		0.5	2.01	2.01	2.01	2.01	2.06
		1.0	2.06	2.06	2.01	2.01	2.06
		2.0	2.06	2.06	2.10	2.06	2.06
10	Low Ratio $T/T_b$ (K/K) = 0.90	0.1	2.00	2.06	2.01	2.01	2.06
		0.5	2.01	2.06	2.01	2.01	2.01
		1.0	2.06	2.06	2.01	2.01	2.01
		2.0	2.04	2.10	2.04	1.96	2.06
	High Ratio $T/T_b$ (K/K) = 0.95	0.1	2.01	2.01	1.96	2.01	2.01
		0.5	2.01	2.01	2.01	2.01	2.01
		1.0	2.01	2.01	2.01	2.10	2.01
		2.0	2.06	2.06	2.06	2.06	2.01

**Table 4.2: Results of vertical integration of intensity for (111) Bragg peaks**

Concentration (mg/mL)	Shearing Temperature (°C)	Shearing Speed (mm/s)	Peak position Chloroform (nm <sup>-1</sup> )	Peak position Benzene (nm <sup>-1</sup> )	Peak position Toluene (nm <sup>-1</sup> )	Peak position m-Xylene (nm <sup>-1</sup> )	Peak position Mesitylene (nm <sup>-1</sup> )
5	Low Ratio $T/T_b$ (K/K) = 0.90	0.1	13.55	13.53	13.69	13.36~13.40	13.41
		0.5		13.53	13.58	13.33~13.45	13.32~13.60
		1.0	13.70		13.65~13.70	13.43	13.38
		2.0	13.30	13.49	13.41~13.53	13.67	13.56
	High Ratio $T/T_b$ (K/K) = 0.95	0.1	13.75	13.54	13.62	13.49	13.48~13.61
		0.5		13.53	13.37	13.38~13.60	13.53~13.69
		1.0			13.21	13.29	13.50~13.62
		2.0		13.60	13.38	13.41	13.42
10	Low Ratio $T/T_b$ (K/K) = 0.90	0.1	13.47~13.75	13.44		13.80	13.76~13.81
		0.5	13.38~13.79			13.25~13.79	13.37
		1.0			13.43	13.27~13.75	13.34
		2.0		13.43	13.38	13.37	13.42
	High Ratio $T/T_b$ (K/K) = 0.95	0.1	13.40	13.43~13.63	13.75	13.60	13.51
		0.5		13.77	13.35	13.48	13.52
		1.0			13.38~13.64	13.32~13.60	13.54
		2.0		13.49	13.27~13.70	13.63	13.51~13.64

**Table 4.3: Results of vertical integration of intensity for (020) Bragg peaks**

Concentration (mg/mL)	Shearing Temperature (°C)	Shearing Speed (mm/s)	Peak position Chloroform (nm <sup>-1</sup> )	Peak position Benzene (nm <sup>-1</sup> )	Peak position Toluene (nm <sup>-1</sup> )	Peak position m-Xylene (nm <sup>-1</sup> )	Peak position Mesitylene (nm <sup>-1</sup> )
5	Low Ratio $T/T_b$ (K/K) = 0.90	0.1	16.18	16.29			16.27~16.32
		0.5		16.34	16.44~16.58	16.18	16.28~16.42
		1.0			16.13~16.38	16.07	16.22
		2.0	16.28	16.33	16.47	16.27	16.38
	High Ratio $T/T_b$ (K/K) = 0.95	0.1	16.28	16.43		16.18	16.34~16.55
		0.5		16.39		16.26~16.40	16.23~16.55
		1.0	16.33~16.40		16.45	16.20	16.22, 16.66*
		2.0	*	16.44		16.07	16.19
10	Low Ratio $T/T_b$ (K/K) = 0.90	0.1	15.98~16.60	16.31~16.37			16.24~16.26
		0.5	16.55	16.71		16.05~16.53	16.10, 16.67*
		1.0	*	16.24	16.19	16.18~16.44	16.08~16.18
		2.0	*	16.28		16.07~16.17	16.22
	High Ratio $T/T_b$ (K/K) = 0.95	0.1	16.49	16.19~16.36, 16.53~16.81*	*	16.16~16.19, 16.68	16.50
		0.5		16.82	16.22~16.57	16.39	16.11~16.48
		1.0			16.54	16.23~16.42	16.54
		2.0	16.26	16.40		16.23	16.33~16.42

\* Coexistence of two polymorphs discerned

**Table 4.4: Effect of temperature on polymorphism by analysis of (111) Bragg peaks**

Solvent	Shearing Speed (mm/s)	Concentration (mg/mL)	Shearing Temperature (°C)	Peak shift direction (+: higher $q_{xy}$ -: lower $q_{xy}$ =: no shift)
Chloroform	0.1	5	28 → 45	+
	0.1	10		-
	0.5	10		-
Benzene	0.1	5	45 → 62	+
	0.5	5		=
	2.0	5		+
	0.1	10		+
	2.0	10		+
Toluene	0.1	5	72 → 91	-
	0.5	5		-
	1.0	5		-
	2.0	5		-
<i>m</i> -Xylene	0.1	5	98 → 118	+
	1.0	5		-
	2.0	5		-
	0.1	10		-
	2.0	10		+
Mesitylene	0.1	5	121 → 143	+
	1.0	5		+
	2.0	5		-
	0.1	10		-
	0.5	10		+
	1.0	10		+
	2.0	10		+

**Table 4.5: Effect of temperature on polymorphism by analysis of (020) Bragg peaks**

Solvent	Shearing Speed (mm/s)	Concentration (mg/mL)	Shearing Temperature (°C)	Peak shift direction (+: higher $q_{xy}$ .: lower $q_{xy}$ =: no shift)
Chloroform	0.1	5	28 → 45	+
	0.5	5		-
	1.0	5		+
	2.0	5		+
Benzene	0.1	5	45 → 62	+
	0.5	5		+
	1.0	5		+
	2.0	5		+
	0.5	10		+
	2.0	10		+
Toluene	2.0	5	72 → 91	+
	2.0	10		+
<i>m</i> -Xylene	0.5	5	98 → 118	+
	1.0	5		+
	2.0	5		-
	0.1	10		-
	2.0	10		+
Mesitylene	0.1	5	121 → 143	+
	2.0	5		-
	0.1	10		+
	1.0	10		+
	2.0	10		+

**Table 4.6: Effect of concentration on polymorphism by analysis of (111) Bragg peaks**

<b>Solvent</b>	<b>Shearing Speed (mm/s)</b>	<b>Shearing Temperature (°C)</b>	<b>Concentration (mg/mL)</b>	<b>Peak shift direction (+: higher <math>q_{xy}</math> .: lower <math>q_{xy}</math> =: no shift)</b>
Chloroform	0.1	28		+
	0.1	45	5 → 10	-
	0.5	45		-
Benzene	0.1	45		-
	2.0	45	5 → 10	-
	0.5	62		+
	2.0	62		-
Toluene	1.0	72		-
	2.0	72		-
	0.1	91	5 → 10	+
	0.5	91		-
	1.0	91		+
<i>m</i> -Xylene	0.1	98		+
	2.0	98		-
	0.1	118	5 → 10	+
	1.0	118		+
	2.0	118		+
Mesitylene	0.1	121		+
	1.0	121	5 → 10	-
	2.0	121		-
	2.0	143		+

**Table 4.7: Effect of concentration on polymorphism by analysis of (020) Bragg peaks**

<b>Solvent</b>	<b>Shearing Speed (mm/s)</b>	<b>Shearing Temperature (°C)</b>	<b>Concentration (mg/mL)</b>	<b>Peak shift direction (+: higher <math>q_{xy}</math> -: lower <math>q_{xy}</math> =: no shift)</b>
Chloroform	0.5	28		-
	0.1	45	5 → 10	+
	1.0	45		-
Benzene	0.1	45		+
	0.5	45		+
	2.0	45	5 → 10	-
	0.5	62		+
	1.0	62		+
	2.0	62		-
Toluene	0.5	72		-
	1.0	72	5 → 10	-
	2.0	91		+
<i>m</i> -Xylene	1.0	98		+
	2.0	98	5 → 10	-
	1.0	118		+
	2.0	118		+
Mesitylene	0.1	121		-
	1.0	121	5 → 10	-
	2.0	121		-
	2.0	143		+

## 5. Results and Discussion III: Solution Processing of Cu(TCNQ)

### 5.1 Batch Synthesis of Two Polymorphs

A combination of PXRD patterns and SEM images shows that two different polymorphs were successfully synthesized. As shown in Figure 5.1 and 5.2, the experimental PXRD patterns were repeated for multiple batches using the same synthesis procedure and compared with reference PXRD patterns [56, 57, 59] to determine which phase was present. SEM images show that Polymorph I is needle-like with the longest dimension about 10  $\mu\text{m}$  long and Polymorph II is platelet-like with the bottom surface about  $5 \times 5 \mu\text{m}^2$  and 2  $\mu\text{m}$  in height.

According to the previous study [56], both polymorphs bear the charge transport properties of a semiconductor. Polymorph I is a relatively good semiconductor with the conductivity of  $0.25 \text{ S cm}^{-1}$  whereas Polymorph II is a relatively poor semiconductor with the conductivity of  $1.3 \times 10^{-5} \text{ S cm}^{-1}$ . Bandgap values are reported as 0.137 eV and 0.332 eV for Polymorph I and II, respectively. All measurements are conducted under room temperature [56]. In addition, an *in operando* X-ray diffraction test conducted by Fernandez et al. has revealed that the phase transition may take place by tuning the applied electric field and an intermediate phase was proposed in the process [57].

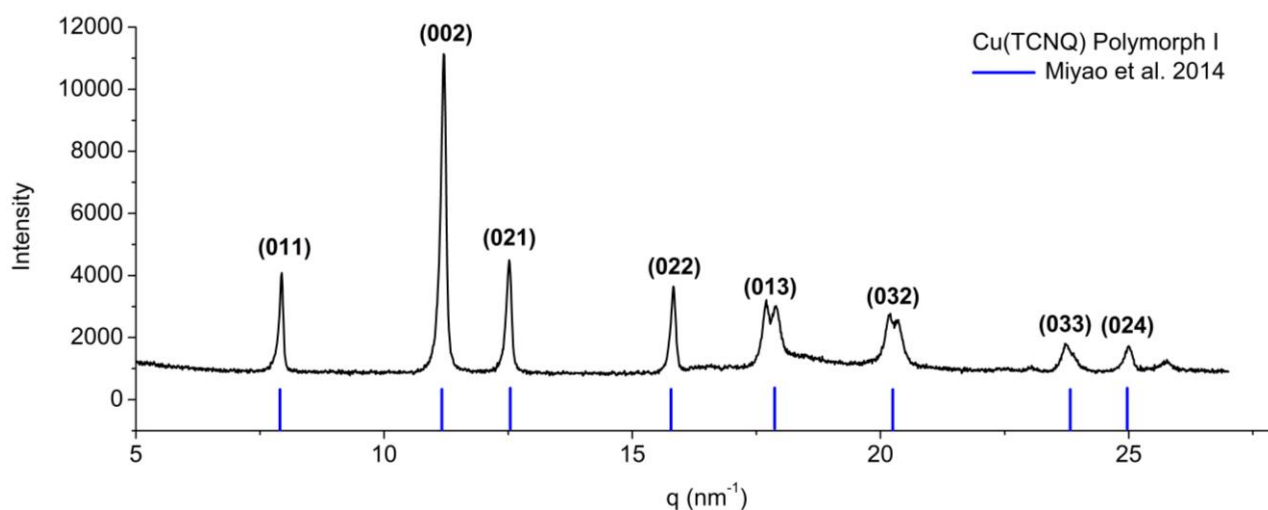
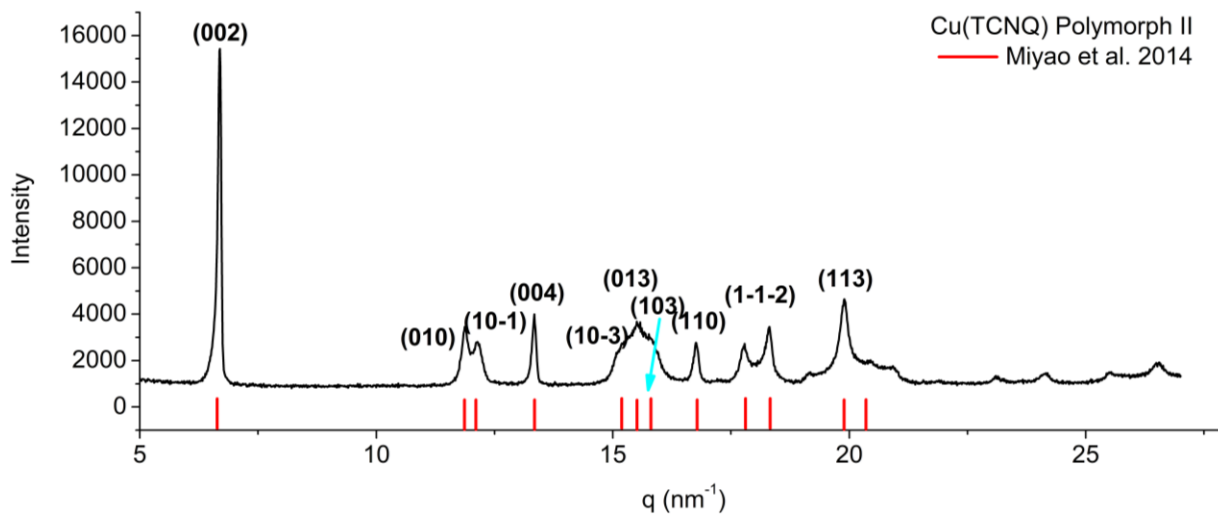
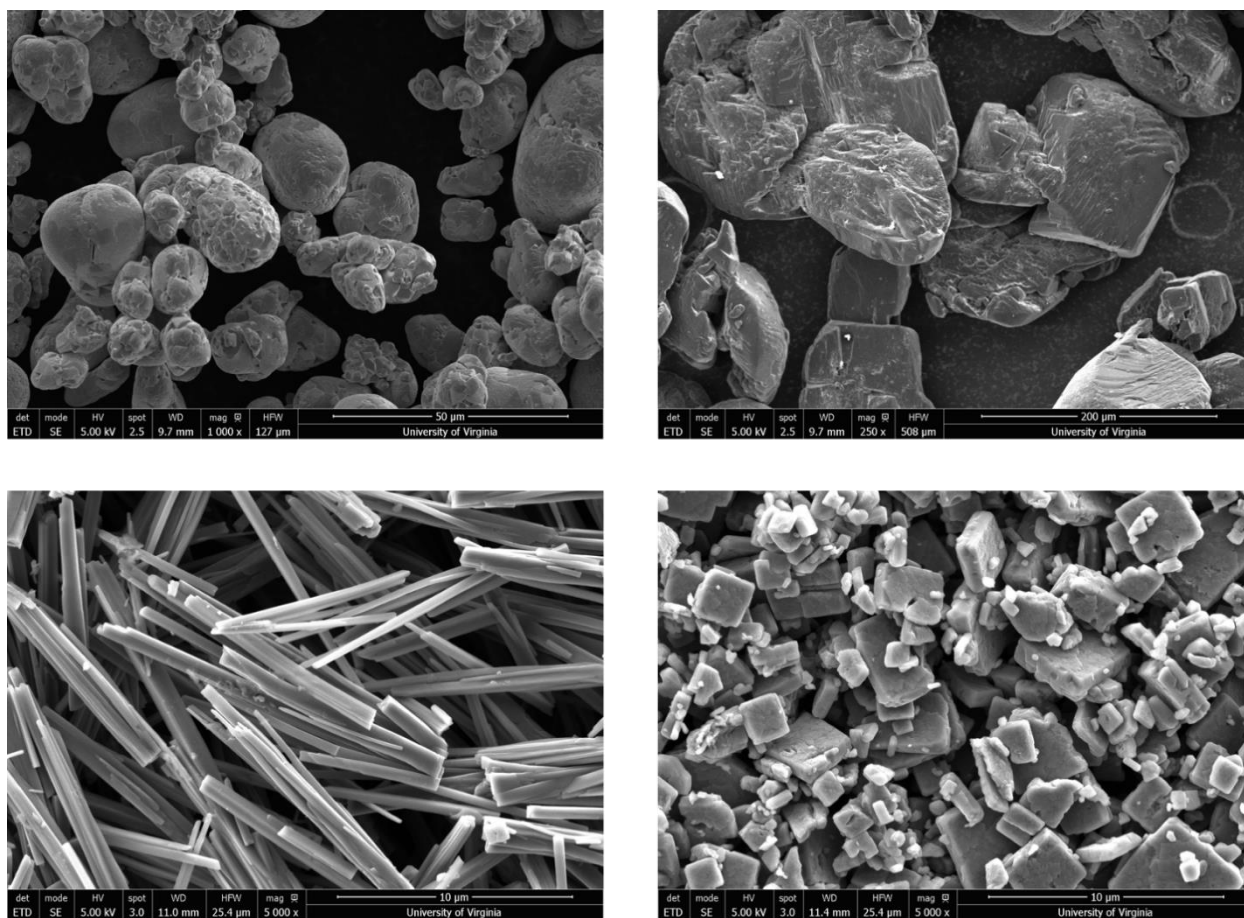


Figure 5.1: PXRD pattern of Cu(TCNQ) Polymorph I.

ATR-FTIR was also used to characterize the two Cu(TCNQ) polymorphs. As shown in Figure 5.4, Polymorph I shows a strong and broad IR absorption at  $2195\text{ cm}^{-1}$  while Polymorph II shows a strong and sharp stretch at  $2207\text{ cm}^{-1}$  with a shoulder at lower wavenumber. The IR spectra are consistent with what has been reported, which is an indicator of getting two distinct Cu(TCNQ) polymorphs.



**Figure 5.2: PXRD pattern of Cu(TCNQ) Polymorph II.**



**Figure 5.3: SEM images of starting materials and two polymorph products in Cu(TCNQ) batch synthesis.** Top left: starting material CuI at 1000X; Top right: starting material TCNQ at 250X; Bottom left: Cu(TCNQ) Polymorph I at 5000X; Bottom right: Cu(TCNQ) Polymorph II at 5000X; All images were taken under secondary electron mode.

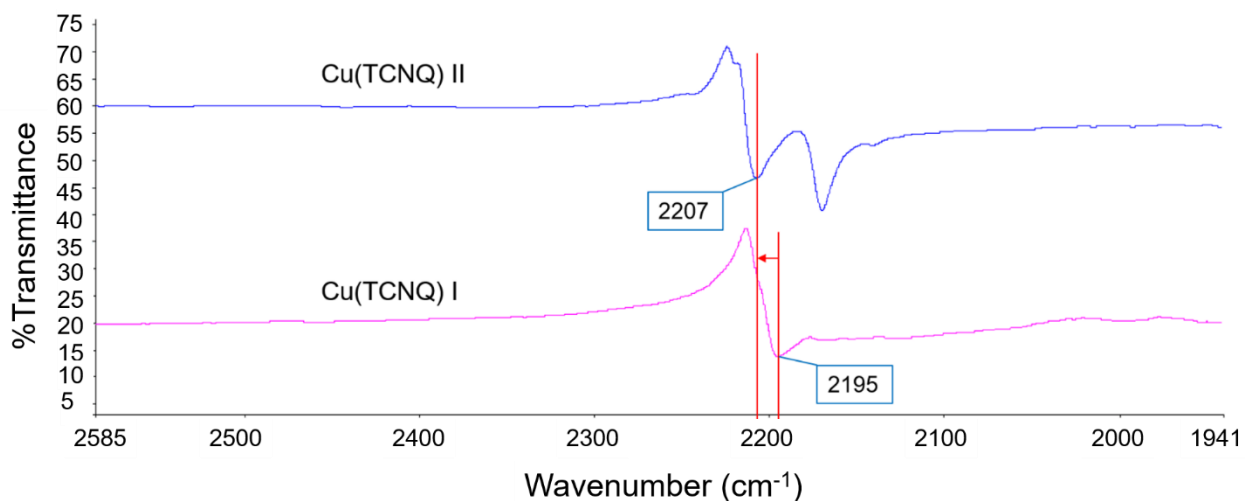


**Figure 5.4: ATR-FTIR spectra of two polymorph products in Cu(TCNQ) batch synthesis.**

In conclusion, the fast kinetics of the reaction to get Polymorph I indicate I is a kinetic product and further exclusive conversion to Polymorph II under room temperature indicates II is a thermodynamic product. The two distinct, stable polymorphs and difference in their conductivity are promising for solution processing of electro-active and electro-switching devices.

## 5.2 BET Analysis

The BET analysis results of Cu(TCNQ) Polymorph I are shown in Figure 5.5. The BET surface area calculated is  $10.9 \pm 0.5 \text{ m}^2/\text{g}$ , which indicates the non-porous nature of Cu(TCNQ) Polymorph I. Same BET analysis procedure was applied to different batches and similar results were obtained.

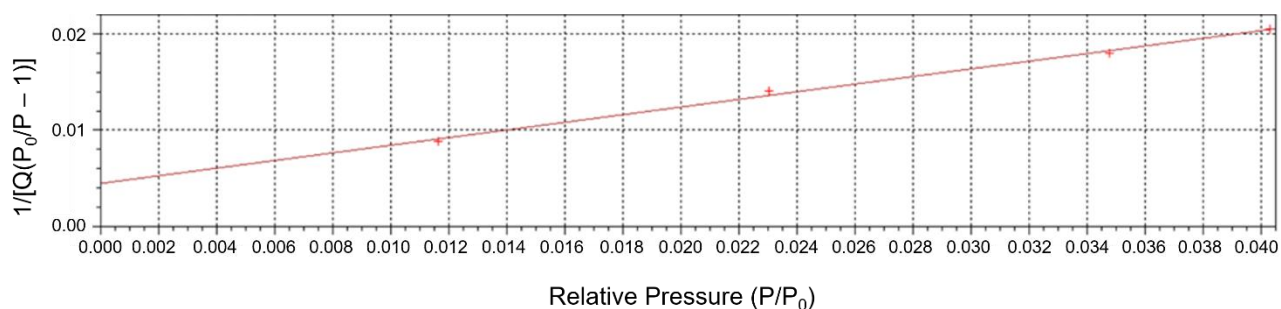


**Figure 5.5: BET surface area plot of Cu(TCNQ) Polymorph I.**

The BET analysis results of Cu(TCNQ) Polymorph II are shown in Figure 5.6. The BET surface area calculated is  $4.0 \pm 0.1 \text{ m}^2/\text{g}$ , which indicates the non-porous nature of Cu(TCNQ) Polymorph II. Same BET analysis procedure was applied to different batches and similar results were obtained. The adsorption isotherm of Polymorph II looks abnormal due to the machine's inherent error. These results indicate that both polymorphs are nonporous and cannot be utilized for gas storage.

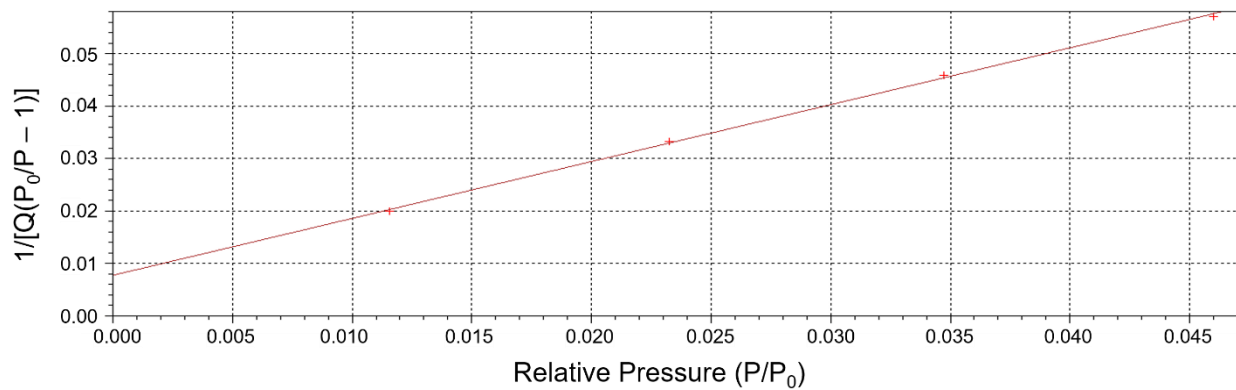


**Figure 5.6: BET surface area plot of Cu(TCNQ) Polymorph II.**

### 5.3 Thin Film Experiment

Growing from copper foil in acetonitrile solution of TCNQ is another route to get Cu(TCNQ). As shown in Figure 5.7 and 5.8, the crystal shape is like an intermediate between Polymorph I and Polymorph II and as the growth time increases, the crystal becomes larger. The result is very promising for the possibility of applying solution shearing method to form Cu(TCNQ) thin films and control polymorphs. Future work includes control of both thin film orientation which can be validated by GIXD and polymorphism since Polymorph I has better conductivity but batch synthesis shows I is a kinetic product and II is a more stable product thermodynamically.

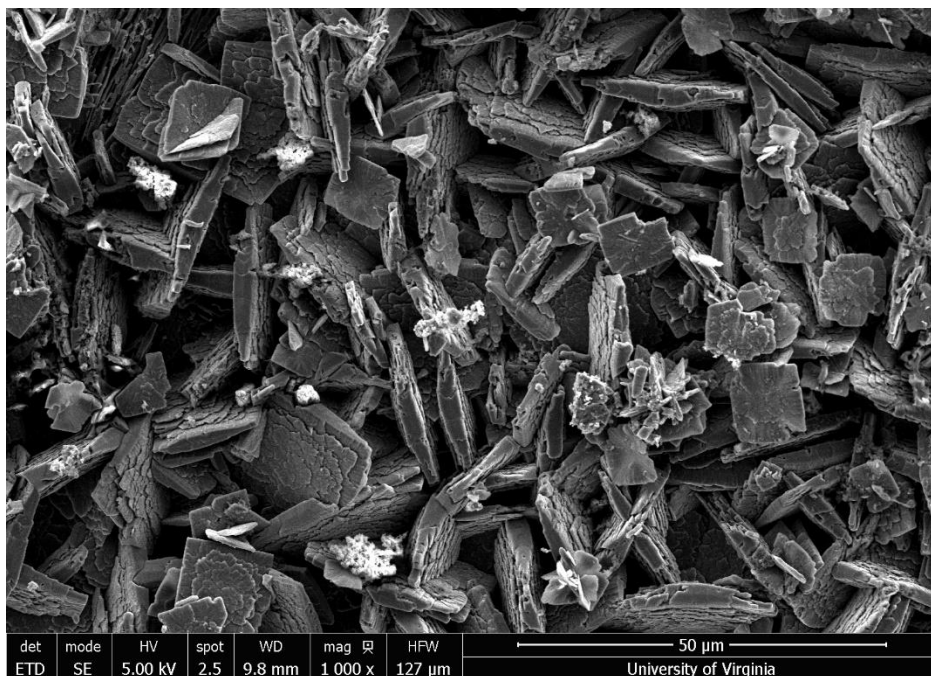


**Figure 5.7:** SEM image Cu(TCNQ) growth on Cu foil in acetonitrile solution of TCNQ at 40 °C for 1 h.



**Figure 5.8:** SEM image Cu(TCNQ) growth on Cu foil in acetonitrile solution of TCNQ at 40 °C for 4 h.

## 6. Conclusions

In this study, an electro-active organic semiconductor candidate C8-BTBT and an electro-active metal organic framework candidate Cu(TCNQ) were selected according to high charge carrier mobility and were prepared using solution process. Based upon previous work, C8-BTBT was processed into thin films using solution shearing method under different processing conditions and thin film morphology and polymorphism were studied. Two distinct and stable polymorphs were synthesized and validated for Cu(TCNQ). Despite proof of non-porous nature, Cu(TCNQ) can be further processed using solution shearing method and fabricated into thin film devices. Thin film orientation study by GIXD may find out optimal conditions for superior conductivity and unveil the effect of solution shearing method on particulate thin film formation. Polymorphism study may correlate shearing conditions to distinct phases and become the kick-off of MOF thin film polymorphism control study in the MOF field.

The following conclusion are drawn:

1. Solution shearing method proves to be a superior solution process to form full-coverage and aligned C8-BTBT thin films.
2. Solution process conditions such as shearing speed, temperature and concentration play a key role in the morphology of C8-BTBT thin films, which may affect the charge carrier mobility of the OSC device.
3. Fluid dynamics and two deposition regimes can be used to explain good thin film morphology is present when sheared under low speed and high temperature.
4. Different polymorphs may form under different shearing conditions and represent distinct charge carrier mobilities. Different theories such as kinetic trapping and vertical 1-D confinement have been used to explain the control of polymorph formation. In-situ GIXD is a powerful tool to capture these metastable phases and validate different hypotheses.

5. To get good charge carrier mobility, morphology control and polymorphism control should both be considered and sometimes may be a tradeoff.
6. Solvent dependent polymorphism is shown to exist in solution-sheared C8-BTBT thin films. Solvent molecular volume can be correlated to the unit cell expansion/contraction direction but other factors such as solvent-solute interaction may be also involved when using different solvents. The GIXD beam footprint, GIXD image resolution and exclusion of effects of other solution process parameters are the obstacles for polymorphism study.
7. Cu(TCNQ) has two distinct and stable polymorphs. Polymorph I is a kinetic phase while Polymorph II is a thermodynamic phase. The two polymorphs also distinguish from each other in conductivities. This property makes Cu(TCNQ) a good candidate for solution shearing of MOF thin films although it is nonporous.

## References

1. Bao, Z. and J. Locklin, *Organic field-effect transistors*. 2007: CRC press.
2. Giri, G., *Understanding and tuning organic semiconductor packing during solution processing*, Z. Bao, G.G. Fuller, and A. Salleo, Editors. 2013.
3. Dimitrakopoulos, C.D. and P.R.L. Malenfant, *Organic thin film transistors for large area electronics*. *Advanced Materials*, 2002. **14**(2): p. 99-+.
4. Diao, Y., et al., *Solution coating of large-area organic semiconductor thin films with aligned single-crystalline domains*. *Nature Materials*, 2013. **12**(7): p. 665-671.
5. Li, H.Y., et al., *Toward high-mobility organic field-effect transistors: Control of molecular packing and large-area fabrication of single-crystal-based devices*. *Mrs Bulletin*, 2013. **38**(1): p. 34-42.
6. Smilgies, D.M., et al., *Look fast: Crystallization of conjugated molecules during solution shearing probed in-situ and in real time by X-ray scattering*. *physica status solidi (RRL)-Rapid Research Letters*, 2013. **7**(3): p. 177-179.
7. Giri, G., et al., *Effect of Solution Shearing Method on Packing and Disorder of Organic Semiconductor Polymers*. *Chemistry of Materials*, 2015. **27**(7): p. 2350-2359.
8. Park, S., et al., *Large-area formation of self-aligned crystalline domains of organic semiconductors on transistor channels using CONNECT*. *Proceedings of the National Academy of Sciences of the United States of America*, 2015. **112**(18): p. 5561-5566.
9. WIKIBOOKS. *Semiconductors/What is a Semiconductor*. 2017 Aug 10, 2017]; Available from: [https://en.wikibooks.org/wiki/Semiconductors/What\\_is\\_a\\_Semiconductor](https://en.wikibooks.org/wiki/Semiconductors/What_is_a_Semiconductor).
10. Bredas, J.L., et al., *Organic semiconductors: A theoretical characterization of the basic parameters governing charge transport*. *Proceedings of the National Academy of Sciences of the United States of America*, 2002. **99**(9): p. 5804-5809.
11. Podzorov, V., et al., *Single-crystal organic field effect transistors with the hole mobility  $\sim 8$  cm<sup>2</sup>/V s*. *Applied Physics Letters*, 2003. **83**(17): p. 3504-3506.

12. Stassen, A., et al., *Influence of the gate dielectric on the mobility of rubrene single-crystal field-effect transistors*. Applied Physics Letters, 2004. **85**(17): p. 3899-3901.
13. Takeya, J., et al., *Very high-mobility organic single-crystal transistors with in-crystal conduction channels*. Applied Physics Letters, 2007. **90**(10): p. 102120.
14. Saeki, A., et al., *Mobility and Dynamics of Charge Carriers in Rubrene Single Crystals Studied by Flash-Photolysis Microwave Conductivity and Optical Spectroscopy*. Advanced Materials, 2008. **20**(5): p. 920-923.
15. Anthony, J.E., et al., *Functionalized pentacene: improved electronic properties from control of solid-state order*. Journal of the American Chemical Society, 2001. **123**(38): p. 9482-9483.
16. Cornil, J., J.P. Calbert, and J.-L. Brédas, *Electronic structure of the pentacene single crystal: Relation to transport properties*. Journal of the American Chemical Society, 2001. **123**(6): p. 1250-1251.
17. Briseno, A.L., et al., *Patterning organic single-crystal transistor arrays*. Nature, 2006. **444**(7121): p. 913.
18. Coropceanu, V., et al., *Charge transport in organic semiconductors*. Chemical Reviews, 2007. **107**(4): p. 926-952.
19. Minemawari, H., et al., *Inkjet printing of single-crystal films*. Nature, 2011. **475**(7356): p. 364-367.
20. Yuan, Y.B., et al., *Ultra-high mobility transparent organic thin film transistors grown by an off-centre spin-coating method*. Nature Communications, 2014. **5**.
21. Uemura, T., et al., *Very High Mobility in Solution-Processed Organic Thin-Film Transistors of Highly Ordered [1]Benzo[thieno[3,2-b]benzothiophene Derivatives*. Applied Physics Express, 2009. **2**(11).
22. Izawa, T., E. Miyazaki, and K. Takimiya, *Molecular Ordering of High-Performance Soluble Molecular Semiconductors and Re-evaluation of Their Field-Effect Transistor Characteristics*. Advanced Materials, 2008. **20**(18): p. 3388-3392.

23. Kumatani, A., et al., *Solution-processed, Self-organized Organic Single Crystal Arrays with Controlled Crystal Orientation*. Scientific Reports, 2012. **2**.
24. Wan, J., et al., *Transient phases during fast crystallization of organic thin films from solution*. Appl Materials, 2016. **4**(1).
25. Diao, Y., et al., *Morphology control strategies for solution-processed organic semiconductor thin films*. Energy & Environmental Science, 2014. **7**(7): p. 2145-2159. - Published by The Royal Society of Chemistry.
26. Niazi, M.R., et al., *Solution-printed organic semiconductor blends exhibiting transport properties on par with single crystals*. Nature Communications, 2015. **6**.
27. Zhang, F., et al., *Ultrathin Film Organic Transistors: Precise Control of Semiconductor Thickness via Spin-Coating*. Advanced Materials, 2013. **25**(10): p. 1401-1407.
28. James, D.T., et al., *Thin-Film Morphology of Inkjet-Printed Single-Droplet Organic Transistors Using Polarized Raman Spectroscopy: Effect of Blending TIPS-Pentacene with Insulating Polymer*. Acs Nano, 2011. **5**(12): p. 9824-9835.
29. Azarova, N.A., et al., *Fabrication of organic thin-film transistors by spray-deposition for low-cost, large-area electronics*. Organic Electronics, 2010. **11**(12): p. 1960-1965.
30. Giri, G., et al., *Tuning charge transport in solution-sheared organic semiconductors using lattice strain*. Nature, 2011. **480**(7378): p. 504-U124.
31. Hamilton, B.D., M.A. Hillmyer, and M.D. Ward, *Glycine polymorphism in nanoscale crystallization chambers*. Crystal Growth & Design, 2008. **8**(9): p. 3368-3375.
32. Ha, J.M., et al., *Polymorph selectivity under nanoscopic confinement*. Journal of the American Chemical Society, 2004. **126**(11): p. 3382-3383.
33. Giri, G., et al., *One-dimensional self-confinement promotes polymorph selection in large-area organic semiconductor thin films*. Nature Communications, 2014. **5**. Copyright (2014) Nature Publishing Group.

34. Hiszpanski, A.M. and Y.L. Loo, *Directing the film structure of organic semiconductors via post-deposition processing for transistor and solar cell applications*. Energy & Environmental Science, 2014. **7**(2): p. 592-608. - Reproduced by permission of The Royal Society of Chemistry.
35. Molina-Lopez, F., et al., *Electric Field Tuning Molecular Packing and Electrical Properties of Solution-Shearing Coated Organic Semiconducting Thin Films*. Advanced Functional Materials, 2017. **27**(8): p. 1605503-n/a.
36. James, S.L., *Metal-organic frameworks*. Chemical Society Reviews, 2003. **32**(5): p. 276-288.
37. Long, J.R. and O.M. Yaghi, *The pervasive chemistry of metal-organic frameworks*. Chemical Society Reviews, 2009. **38**(5): p. 1213-1214.
38. Zhou, H.-C., J.R. Long, and O.M. Yaghi, *Introduction to metal-organic frameworks*. 2012, ACS Publications.
39. Kitagawa, S., *Metal-organic frameworks (MOFs)*. Chemical Society Reviews, 2014. **43**(16): p. 5415-5418.
40. Li, H., et al., *Design and synthesis of an exceptionally stable and highly porous metal-organic framework*. Nature, 1999. **402**(6759): p. 276-279.
41. Lee, J., et al., *Metal-organic framework materials as catalysts*. Chemical Society Reviews, 2009. **38**(5): p. 1450-1459.
42. Yaghi, O.M., G.M. Li, and H.L. Li, *Selective Binding and Removal of Guests in a Microporous Metal-Organic Framework*. Nature, 1995. **378**(6558): p. 703-706.
43. Horcajada, P., et al., *Porous metal-organic-framework nanoscale carriers as a potential platform for drug delivery and imaging*. Nature Materials, 2010. **9**(2): p. 172-178.
44. Chen, B., et al., *High H<sub>2</sub> Adsorption in a Microporous Metal-Organic Framework with Open Metal Sites*. Angewandte Chemie, 2005. **117**(30): p. 4823-4827.
45. Farha, O.K., et al., *De novo synthesis of a metal-organic framework material featuring ultrahigh surface area and gas storage capacities*. Nature Chemistry, 2010. **2**(11): p. 944-948.

46. Millward, A.R. and O.M. Yaghi, *Metal-organic frameworks with exceptionally high capacity for storage of carbon dioxide at room temperature*. Journal of the American Chemical Society, 2005. **127**(51): p. 17998-17999.
47. Sumida, K., et al., *Carbon dioxide capture in metal-organic frameworks*. Abstracts of Papers of the American Chemical Society, 2011. **242**.
48. Horcajada, P., et al., *Metal-organic frameworks as efficient materials for drug delivery*. Angewandte chemie, 2006. **118**(36): p. 6120-6124.
49. Horcajada, P., et al., *Porous metal-organic-framework nanoscale carriers as a potential platform for drug delivery and imaging*. Nature materials, 2010. **9**(2): p. 172.
50. Horcajada, P., et al., *Flexible porous metal-organic frameworks for a controlled drug delivery*. Journal of the American Chemical Society, 2008. **130**(21): p. 6774-6780.
51. Talin, A.A., et al., *Tunable electrical conductivity in metal-organic framework thin-film devices*. Science, 2013: p. 1246738.
52. Ma, D., et al., *A dual functional MOF as a luminescent sensor for quantitatively detecting the concentration of nitrobenzene and temperature*. Chemical Communications, 2013. **49**(79): p. 8964-8966.
53. Wang, J.-H., M. Li, and D. Li, *A dynamic, luminescent and entangled MOF as a qualitative sensor for volatile organic solvents and a quantitative monitor for acetonitrile vapour*. Chemical Science, 2013. **4**(4): p. 1793-1801.
54. Liverpool, U.o. *HKUST-1 Metal Organic Framework*. 2008-2017 Aug 10, 2017]; Available from: <http://www.chemtube3d.com/solidstate/MOF-HKUST-1.html>. Copyright ChemTube3D by Nick Greeves.
55. Kaye, S.S., et al., *Impact of preparation and handling on the hydrogen storage properties of Zn4O(1,4-benzenedicarboxylate)(3) (MOF-5)*. Journal of the American Chemical Society, 2007. **129**(46): p. 14176-+. Copyright (2007) American Chemical Society

56. Heintz, R.A., et al., *New insight into the nature of Cu(TCNQ): Solution routes to two distinct polymorphs and their relationship to crystalline films that display bistable switching behavior*. Inorganic Chemistry, 1999. **38**(1): p. 144-156.
57. Fernandez, C.A., et al., *An Electrically Switchable Metal-Organic Framework*. Scientific Reports, 2014. **4**. Copyright (2014) Nature Publishing Group.
58. Potember, R., T. Poehler, and D. Cowan, *Electrical switching and memory phenomena in Cu-TCNQ thin films*. Applied Physics Letters, 1979. **34**(6): p. 405-407.
59. Miyao, K., et al., *Reversible iodine absorption of nonporous coordination polymer Cu(TCNQ)*. New Journal of Chemistry, 2014. **38**(2): p. 739-743.
60. Bragg, W.L., *The Diffraction of Short Electromagnetic Waves by a Crystal*. Proceedings of the Cambridge Philosophical Society, 1913. **17**: p. 43-57.
61. WIKIPEDIA. *Bragg's law*. 2017 Aug 10, 2017]; Available from: [https://en.wikipedia.org/wiki/Bragg%27s\\_law](https://en.wikipedia.org/wiki/Bragg%27s_law).
62. Engineering, M.C.f.M.S.a. *X-ray Diffraction Shared Experimental Facility*. 2016 Aug 10, 2017]; Available from: <http://prism.mit.edu/xray/>.
63. Smilgies, D.M., *Scherrer grain-size analysis adapted to grazing-incidence scattering with area detectors*. Journal of Applied Crystallography, 2009. **42**: p. 1030-1034.
64. Birkholz, M., *Thin Film Analysis by X-Ray Scattering*. Thin Film Analysis by X-Ray Scattering, 2006: p. 1-356.
65. Cambridge, U.o. *Optical Microscopy and Specimen Preparation*. n.d. Aug 10, 2017]; Available from: <http://www.icbl.hw.ac.uk/learnem/doitpoms/OpticalMicroscopy/pmicroscopy.htm>.
66. FEI. *Quanta x50 Training Handbook*. 2013 Aug 10, 2017]; Available from: <http://www.virginia.edu/ms/nmcf/pdfs/restricted/Quantra%20Training%20Manual.pdf>.
67. PerkinElmer. *FT-IR Spectroscopy Attenuated Total Reflectance (ATR)*. n.d. Aug 10, 2017]; Available from: [https://shop.perkinelmer.com/content/TechnicalInfo/TCH\\_FTIRATR.pdf](https://shop.perkinelmer.com/content/TechnicalInfo/TCH_FTIRATR.pdf).

68. Le Berre, M., Y. Chen, and D. Baigl, *From Convective Assembly to Landau-Levich Deposition of Multilayered Phospholipid Films of Controlled Thickness*. *Langmuir*, 2009. **25**(5): p. 2554-2557.